



**UNIVERSITY OF LEEDS**

This is a repository copy of *Influence of multiphase turbulence modelling on interfacial momentum transfer in two-fluid Eulerian-Eulerian CFD models of bubbly flows*.

White Rose Research Online URL for this paper:  
<http://eprints.whiterose.ac.uk/140317/>

Version: Accepted Version

---

**Article:**

Colombo, M and Fairweather, M (2019) Influence of multiphase turbulence modelling on interfacial momentum transfer in two-fluid Eulerian-Eulerian CFD models of bubbly flows. *Chemical Engineering Science*, 195. pp. 968-984. ISSN 0009-2509

<https://doi.org/10.1016/j.ces.2018.10.043>

---

© 2018 Elsevier Ltd. This manuscript version is made available under the CC-BY-NC-ND 4.0 license <http://creativecommons.org/licenses/by-nc-nd/4.0/>.

**Reuse**

This article is distributed under the terms of the Creative Commons Attribution-NonCommercial-NoDerivs (CC BY-NC-ND) licence. This licence only allows you to download this work and share it with others as long as you credit the authors, but you can't change the article in any way or use it commercially. More information and the full terms of the licence here: <https://creativecommons.org/licenses/>

**Takedown**

If you consider content in White Rose Research Online to be in breach of UK law, please notify us by emailing [eprints@whiterose.ac.uk](mailto:eprints@whiterose.ac.uk) including the URL of the record and the reason for the withdrawal request.



[eprints@whiterose.ac.uk](mailto:eprints@whiterose.ac.uk)  
<https://eprints.whiterose.ac.uk/>

# **Influence of multiphase turbulence modelling on interfacial momentum transfer in two-fluid Eulerian-Eulerian CFD models of bubbly flows**

**Marco Colombo\* and Michael Fairweather**

School of Chemical and Process Engineering, University of Leeds, Leeds LS2 9JT, UK

\*Corresponding Author: [M.Colombo@leeds.ac.uk](mailto:M.Colombo@leeds.ac.uk); +44 (0) 113 343 2351

## **ABSTRACT**

Eulerian-Eulerian two-fluid computational fluid dynamic (CFD) models are increasingly used to predict bubbly flows at an industrial scale. In these approaches, interface transfer is modelled with closure models and correlations. Normally, the lateral void fraction distribution is considered to mainly result from a balance between the lift and wall lubrication forces. However, and despite the numerous models available that achieve, at least in pipe flows, a reasonable predictive accuracy, agreement on a broadly applicable and accurate modelling approach has not yet been reached. Additionally, the impact of turbulence modelling on the lateral void fraction distribution has not, in general, been examined in detail. In this work, an elliptic blending Reynolds stress model (EB-RSM), capable of resolving the turbulence field in the near-wall region and improved to account for the contribution of bubble-induced turbulence, is evaluated against best-practice  $k$ - $\varepsilon$  and high-Reynolds second-moment turbulence closures. Lift and wall lubrication forces are initially deliberately neglected in the EB-RSM. Comparisons for flows in pipes and a square duct show that the EB-RSM reproduces the lateral void fraction distribution, including the peak in the void fraction in the near-wall region, and reaches an accuracy comparable to the other two models noted above. In rod bundles, even if none of the models considered performs with sufficient accuracy, the EB-RSM detects features of the flow that are not predicted by the other two approaches. Overall, the results demonstrate a much more prominent role of the turbulence structure and the induced cross-sectional pressure field on the lateral void fraction distribution than is normally considered. These effects need to be accounted for if more physically-consistent modelling of bubbly flows is to be achieved. The lift force is added to the EB-RSM in the final part of the paper, to provide a two-fluid formulation that can be used as the basis for additional developments aimed at improving the accuracy and general applicability of two-fluid CFD models.

**Keywords:** bubbly flow; two-fluid model; multiphase turbulence; Reynolds stress turbulence; elliptic blending; void fraction distribution.

## 1. Introduction

Multiphase gas-liquid bubbly flows are frequently encountered in nature and are common in industry and engineering applications, for example in heat exchangers, bubble column reactors, nuclear reactors and in many oil and gas applications. Bubbles strongly affect the flow of the continuous liquid phase and quantities such as the interfacial area concentration and the volume fraction of the gas phase drive the design and operation of industrial equipment. Therefore, research has been ongoing for many years to develop improved and more accurate models of bubbly flows. Over the years, numerous experiments have been conducted. The continual improvement of measurement techniques has made available progressively more detailed and accurate experimental data. Serizawa et al. (1975) studied experimentally air-water upward flows in a 60 mm inner diameter (ID) pipe at atmospheric pressure. Experiments in air-water bubbly upward flows were also made by Liu and Bankoff (1993a, b) in a 38 mm ID pipe. In both works, bubble velocity and diameter were measured with a two-sensor electrical resistivity probe and liquid velocity and turbulence by hot-film anemometer probes. Talley et al. (2015) measured bubble velocity, void fraction, interfacial area concentration and Sauter-mean diameter in a 38.1 mm ID horizontal pipe using a four-sensor conductivity probe. Kim et al. (2016) measured liquid and gas velocity and turbulent stresses in a 40 mm ID vertical pipe using the two-phase particle image velocimetry technique. A few decades ago, mathematical models were mainly limited to correlations or one-dimensional methods for predicting area-averaged values of the interfacial area concentration or the void fraction (Ohkawa and Lahey, 1980; Coddington and Macian, 2002; Woldesemayat and Ghajar, 2007; Vasavada et al., 2009). However, bubbly flows and multiphase gas-liquid flows in more general are multiscale in nature, which constrains the modelling approaches above to mainly empirical treatments and limited accuracy and applicability. To provide an example, coalescence of bubbles is governed by trap, drainage and rupture of liquid films of micrometer thickness (Prince and Blanch, 1990; Liao and Lucas, 2010). These microscale phenomena drive the formation of larger bubbles and the evolution of the bubble diameter distribution strongly affects the average flow and the gas-phase concentration at the component-scale level. The ability to handle such small-scale phenomena in large, component-scale simulations has driven the recent development of computational fluid dynamic (CFD) models, which has made possible the calculation of detailed three-dimensional void fraction and interfacial area distribution fields (Yao and Morel, 2004; Nguyen et al., 2013; Rzehak and Krepper, 2013; Colombo and Fairweather, 2016). Interface tracking techniques even allow prediction of the behaviour of individual bubbles in a

flow, though their applicability is still limited to a small number of bubbles due to run time constraints. Dabiri and Tryggvason (2015) simulated a turbulent bubbly flow in a channel at Reynolds numbers up to 5600 and with an imposed constant heat flux. 84 mono-dispersed bubbles were tracked with a front tracking technique, with the void fraction kept constant at 3 % and with density ratio values up to 40. Feng and Bolotnov (2017) evaluated the bubble-induced contribution to single-phase turbulence by resolving the interaction of a single bubble and homogenous turbulence by using direct numerical simulation (DNS) and the level set interface tracking method. Instead, for the prediction of industrial-scale flows, Eulerian-Eulerian averaged two-fluid models have been the most frequent choice (Hosokawa and Tomiyama, 2009; Colombo and Fairweather, 2015; Liao et al., 2015).

In Eulerian-Eulerian two-fluid models, the phases are treated as interpenetrating continua and details of the interface structure are lost in the averaging procedure. Therefore, closure relations are required to model interphase exchanges of mass, momentum and energy. In the majority of studies, drag, lift, wall lubrication and turbulent dispersion forces have been considered to be the dominant momentum coupling terms (Yao and Morel, 2004; Hosokawa and Tomiyama, 2009; Rzehak and Krepper, 2013; Colombo and Fairweather, 2015). In closed ducts, bubbles have been repeatedly observed to obey two types of behaviour. Smaller spherical bubbles tend to migrate towards the duct walls, generating a near-wall peak in the void fraction distribution. Conversely, larger bubbles, whose shape is deformed by the inertia of the surrounding liquid, move towards the centre of the duct. This effect can be attributed to a change in the direction of the lift force, with the critical bubble diameter at which lift turns from positive to negative being in the region of 4 to 6 mm (Tomiyama et al., 2002b; Lucas et al., 2010). As a result, in most of the CFD studies performed to date, the lateral void fraction distribution is essentially obtained from a balance between the lift and wall lubrication forces, with the additional effect of turbulent dispersion working against void fraction gradients. Over the years, numerous lift models have been developed, and many were optimized to predict the wall-peak void fraction distribution observed in bubbly flow experiments in pipes (Serizawa et al., 1975; Liu and Bankoff, 1993a, b). Even so, no general consensus has been reached on the most accurate model, and an abundance of formulations exists (Hibiki and Ishii, 2007). This is because the performance of the lift model is unavoidably related to the value of the other forces present, and the wall lubrication force in particular. For the latter force, an even larger number of slightly different prescriptions is available, with wall lubrication being totally neglected by some authors. Antal et al. (1991) derived their wall force model from theoretical considerations

and assuming a spherical bubble shape and an irrotational flow. Yao and Morel (2004) employed a constant lift coefficient equal to 0.5 and neglected any wall repulsive force. Hosokawa and Tomiyama (2009) adopted the Tomiyama et al. (2002b) model for the lift force and a model of the wall force they had developed a few years earlier (Hosokawa and Tomiyama, 2003). Rzehak and Krepper (2013) modelled the lift force with the Tomiyama et al. (2002b) model and for the wall force the Antal et al. (1991) model with coefficients modified accordingly to the ANSYS CFX implementation. Colombo and Fairweather (2015) employed a constant lift coefficient of 0.1 and the Antal et al. (1991) model with coefficients modified to fit a large database of bubbly flows. Therefore, it is more accurate to say that an abundance of coupled lift-wall lubrication force models exists.

In some recent works, a different and more complex structure of interfacial momentum transfer has been identified and discussed. Ullrich et al. (2014) demonstrated the possibility of predicting the near-wall peak of the void fraction profile even when neglecting the lift and wall force contributions. In the authors' pipe flow simulations, the radial pressure gradient, induced by the continuous phase turbulence field, was sufficient to induce the near-wall peak in the gas phase void fraction. The authors employed a near-wall Reynolds stress model (RSM), able to capture the anisotropy of the turbulence structure and the strong effect this has on the radial distribution of the bubbles. This role of the continuous phase turbulence had been rarely considered in previous works, in which multiphase extensions of single-phase linear eddy viscosity models had generally been applied. To provide some examples, Troshko and Hassan (2001), Yao and Morel (2004) and Sugrue et al. (2017) have adopted multiphase extensions of the  $k-\varepsilon$  model, while Rzehak and Krepper (2013) and Liao et al. (2015) employed the SST  $k-\omega$  model. These works, in view of the intrinsic limitations of eddy viscosity-based turbulence models, were unable to correctly predict the three-dimensional turbulence structure and its influence on the void fraction distribution, in particular when, as is often done in single-phase simulations, the turbulence kinetic energy is added to the pressure field. An exception was the studies of Drew and Lahey (1982) and Lopez de Bertodano et al. (1990), which adopted a Reynolds stress model of the turbulence to successfully predict the radial void fraction distribution in circular pipes. Lahey et al. (1993) derived an algebraic RSM that predicted with accuracy bubbly flows in triangular ducts. Recently, Mimouni et al. (2010, 2011) developed an RSM for application in nuclear reactor thermal hydraulics. Comparison with bubbly flow experiments in a  $2 \times 2$  rod bundle show the improved accuracy of the RSM with respect to a  $k-\varepsilon$  model in these conditions. More recently, Santarelli and Frohlich (2015) simulated a

vertical bubbly flow in a channel using DNS and the immersed boundary method. A no-slip boundary condition was applied at the interphase, representing air bubbles rising in water contaminated with surfactants. From simulations of a fixed solid sphere in a shear flow, the authors found that, even with spherical bubbles, the lift force can become negative with an increase in the shear rate and the Reynolds number. This effect was attributed to the asymmetry of the wake behind the sphere in a shear flow. Therefore, the wall-peaked profiles of the void fraction distribution observed in bubbly flows were related to the action of the turbulence, and more specifically to the turbophoresis effect. In a later paper, Santarelli and Frohlich (2016) confirmed their findings with bubbles of different sizes. On increasing the bubble diameter, the void fraction radial distribution was found to assume a core-peaked shape that the authors attributed to a larger negative lift, high enough to overcome the action of turbophoresis. Lubchenko et al. (2018), starting from experimental (Hassan, 2014) and DNS (Lu and Tryggvason, 2013) evidence, questioned the physical basis of the wall lubrication force. Their model predicts the wall-peaked void fraction distribution in pipe flows even without accounting for wall lubrication, when a different formulation of the turbulent dispersion force is employed.

In this paper, modelling of the interphase momentum exchange in a two-fluid Eulerian-Eulerian CFD model and the effect of the continuous phase turbulence field on the lateral void fraction distribution of the dispersed phase are analysed. With respect to the previous works cited above that employed high-Reynolds Reynolds-stress closures, a wall-resolved elliptic-blending Reynolds stress model (EB-RSM) is adopted. The model is coupled to an interphase momentum exchange closure where lift and wall lubrication forces are neglected and only turbulent dispersion is considered in addition to the drag force. Results are compared to more standard approaches based on high-Reynolds number  $k-\varepsilon$  and Reynolds stress turbulence models that include lift and wall force contributions. The models are tested not only in pipes, but also in a square duct and in a rod bundle. Compared to pipes, square ducts and rod bundles have received less attention in the literature, and the accuracy of lift and wall force models in these geometries is much less well established. A selection of experiments characterized by a mono-dispersed bubble size distribution allows the analysis to focus on turbulence and interphase closure modelling. The role of the different interphase forces in a two-fluid model, and of the lift-wall lubrication balance on the lateral void fraction distribution, are discussed. More specifically, the action of the turbulence structure on the void fraction distribution and the benefits of high order turbulence modelling for overall two-fluid model accuracy and

generality are addressed. Finally, the addition of the lift force to the EB-based two-fluid model is evaluated as a basis for further developments in the CFD modelling of bubbly flows.

## 2. Experimental data

Numerical results are compared against air-water bubbly flow experimental data obtained in three geometries, namely a pipe, a square duct and a rod bundle. More specifically, two pipe flows are taken from Liu and Bankoff (1993a) and Hosokawa and Tomiyama (2009), the square duct flow from Sun et al. (2014) and the rod bundle flow from Hosokawa et al. (2014).

Liu and Bankoff (1993a, b) investigated upward air-water bubbly flows inside a vertical pipe of 38 mm inside diameter. Liquid mean velocities and turbulent fluctuations were measured using one and two-dimensional hot-film anemometer probes, and bubble velocity, void fraction and frequency with an electrical resistivity probe. Measurements were taken for 48 flow conditions that covered the ranges  $0.376\text{-}1.391\text{ m s}^{-1}$  for the liquid superficial velocity,  $0.027\text{-}0.347\text{ m s}^{-1}$  for the air superficial velocity and  $0.0\text{-}0.5$  for the void fraction.

Hosokawa and Tomiyama (2009) studied air-water bubbly flows flowing upward in a vertical pipe having an inside diameter of 25 mm. Liquid velocities were measured with using laser Doppler velocimetry and two high-speed cameras were used to obtain stereoscopic images of the bubbles. From these images, the authors reconstructed the bubble number, size and shape, and the bubble velocity. Measurements were obtained in the ranges  $0.5\text{-}1.0\text{ m s}^{-1}$  for the liquid superficial velocity,  $0.018\text{-}0.036\text{ m s}^{-1}$  for the air superficial velocity,  $0.0146\text{-}0.0399$  for the void fraction and  $3.21\text{-}4.25\text{ mm}$  for the bubble diameter.

Sun et al. (2014) measured upward air-water bubbly flows in a vertical square duct having a side length of 0.136 m. X-type hot-film anemometry was used to measure the velocity of the liquid phase and a multi-sensor optical probe and a high-speed camera for measurements in the gas phase. Local values of the void fraction, the bubble diameter and frequency, the mean water velocity and the turbulence kinetic energy were measured for 11 two-phase flow conditions. Measurements were taken along parallel lines in the two directions perpendicular to the duct axis using a resolution of 121 measurement points in each quarter square area of the cross-section. Measurements covered the ranges  $0.5\text{-}1.0\text{ m s}^{-1}$  for the liquid superficial velocity,  $0.045\text{-}0.226\text{ m s}^{-1}$  for the air superficial velocity and  $0.069\text{-}0.172$  for the void fraction.

Hosokawa et al. (2014) experimentally studied upward air-water bubbly flow in a vertical 4×4 rod bundle. The outer diameter of the rods was 10 mm and the pitch 12.5 mm. The rod bundle was contained inside a square box having a side length of 54 mm and a corner radius of 8.25 mm. The void fraction distribution and bubble velocity in various sub-channels were measured by a double-sensor conductivity probe. Liquid velocity was measured using a laser Doppler velocimetry technique. Measurements covered the ranges 0.9-1.5 m s<sup>-1</sup> for the liquid superficial velocity, 0.06-0.15 m s<sup>-1</sup> for the air superficial velocity and 0.0-0.22 for the void fraction.

Initially, results are compared with a pipe flow experiment from Hosokawa and Tomiyama (2009). To extend the comparison to higher void fractions, a pipe flow from Liu and Bankoff (1993a) is subsequently considered. Finally, comparison is made with a flow from the square duct database of Sun et al. (2014) and a flow from the rod bundle database of Hosokawa et al. (2014). Using the information available on the bubble diameter, specific experiments were selected to have bubbles characterized by a homogeneous mono-dispersed size distribution. Bubbles maintain a spherical or slightly deformed shape. Consequently, all the bubbles show a similar behaviour and the population can be effectively characterized by the average diameter of the mono-dispersed distribution (Besagni et al., 2018). This is confirmed by the measured bubble diameter distribution, when available (Liu and Bankoff, 1993b; Hosokawa and Tomiyama, 2009), and by the wall-peaked void profiles recorded in all four experiments. Experimental conditions are summarized in Table 1 and details on the selection of the average bubble diameter in the CFD simulations are provided later in Section 4.

Table 1. Summary of experiments used to assess CFD simulations.

<b>Experiment</b>	<b><math>j_w</math> [m s<sup>-1</sup>]</b>	<b><math>j_a</math> [m s<sup>-1</sup>]</b>	<b>Geometry</b>	<b><math>D_h</math> [m]</b>
Hosokawa and Tomiyama (2009)	1.0	0.036	Pipe	0.025
Liu and Bankoff (1993a)	0.753	0.180	Pipe	0.038
Sun et al. (2014)	0.75	0.09	Square duct	0.136
Hosokawa et al. (2014)	0.9	0.06	4 × 4 Rod bundle	0.009

### 3. CFD model

In the two-fluid Eulerian-Eulerian approach, each phase is described by a set of averaged conservation equations. Adiabatic air-water flows are considered in this work, therefore only the continuity and momentum equations are necessary, with the phases treated as incompressible with constant properties:



$$\frac{\partial}{\partial t}(\alpha_k \rho_k) + \frac{\partial}{\partial x_i}(\alpha_k \rho_k U_{i,k}) = 0 \quad (1)$$

$$\begin{aligned} \frac{\partial}{\partial t}(\alpha_k \rho_k U_{i,k}) + \frac{\partial}{\partial x_j}(\alpha_k \rho_k U_{i,k} U_{j,k}) \\ = -\alpha_k \frac{\partial}{\partial x_i} p_k + \frac{\partial}{\partial x_j} [\alpha_k (\tau_{ij,k} + \tau_{ij,k}^{Re})] + \alpha_k \rho_k g_i + M_{i,k} \end{aligned} \quad (2)$$

In the above equations,  $\alpha_k$  represents the volume fraction of phase  $k$ , whereas in the following  $\alpha$  is used to specify the void fraction of air.  $\rho$  is the density,  $U$  the velocity,  $p$  the pressure and  $g$  the gravitational acceleration.  $\tau$  and  $\tau^{Re}$  are the laminar and turbulent stress tensors, respectively, and  $M_k$  is the interfacial momentum transfer source. When using the EB-RSM, only the drag force and turbulent dispersion force are considered, and the lift and the wall lubrication forces are neglected. In contrast, when the high Reynolds number  $k$ - $\epsilon$  model and RSM are used, the lift and wall contributions are included.

### 3.1. Interfacial momentum transfer

The drag force is an expression of the resistance opposed to bubble motion relative to the surrounding liquid. The model of Tomiyama et al. (2002a), which accounts for the effect of the bubble aspect ratio, is used to predict the drag coefficient  $C_D$ :

$$C_D = \frac{8}{3} \frac{Eo}{E^{2/3}(1 - E^2)^{-1}Eo + 16E^{4/3}} F^{-2} \quad (3)$$

The drag coefficient is a function of the Eötvös number ( $Eo = \Delta\rho g d_B / \sigma$ , where  $\sigma$  is the surface tension) and bubble aspect ratio  $E$ .  $F$  in Eq. (3) is an additional function of the bubble aspect ratio. The bubble aspect ratio is calculated from a correlation and it is function of the distance from the wall  $y_w$ :

$$E = \max \left[ 1.0 - 0.35 \frac{y_w}{d_B}, E_0 \right] \quad (4)$$

Eq. (4) follows experimental evidence that shows that the aspect ratio increases and tends to a value of 1 (perfectly spherical bubble) as the wall is approached. As a consequence, the drag coefficient increases and a reduction in the relative velocity between the bubbles and the fluid is observed in the near-wall region (Hosokawa and Tomiyama, 2009). The reference value  $E_0$  is obtained from the correlation of Welleck et al. (1966). An additional correction is also included to account for drag reduction due to bubble swarm (Tomiyama et al., 1998):

$$C_D = C_{D,0}\alpha^{-0.5} \quad (5)$$

Each bubble moving in a shear flow experiences a lift force perpendicular to its direction of motion. Therefore, the lift force influences the lateral movement of the bubbles and the void fraction distribution. Generally, a positive value of the lift coefficient characterizes spherical bubbles, which are therefore pushed towards the wall. Larger bubbles that are deformed by inertial forces experience a change of sign in the lift force and are pushed towards the centre of the flow (Ervin and Tryggvason, 1997; Tomiyama et al., 2002b). Over the years, numerous models have been proposed. Amongst others, the correlation from Tomiyama et al. (2002b) is frequently used (Rzehak and Krepper, 2013; Liao et al., 2015):

$$C_L = \begin{cases} \min[0.288 \tanh(0.121 Re_b), f(Eo_d)] & Eo_d < 4 \\ f(Eo_d) & 4 < Eo_d < 10 \\ -0.27 & Eo_d > 10 \end{cases} \quad (6)$$

In Eq. (6),  $Re_B$  is the bubble Reynolds number ( $Re_B = \rho_c U_r d_B / \mu_c$ , where the density and viscosity of the continuous phase  $c$  are used, and  $U_r$  is the magnitude of the relative velocity).  $Eo_d$  is a modified Eötvös number where the maximum horizontal dimension of the bubble, obtained using the aspect ratio from Welleck et al. (1966), is employed.  $f(Eo_d)$  is a function of the modified Eötvös number:

$$f(Eo_d) = 0.00105 Eo_d^3 - 0.0159 Eo_d^2 - 0.0204 Eo_d + 0.474 \quad (7)$$

In this work, results are compared against data using a constant value of the lift coefficient  $C_L = 0.1$ , adopted by other researchers who reported good agreement with experimental measurements (Lopez de Bertodano et al., 1994; Lahey and Drew, 2001; Colombo and Fairweather, 2015). In the past, agreement with data has been reported for values of the lift coefficient ranging from 0.01 (Wang et al., 1987; Yeoh and Tu, 2006) to 0.5 (Mimouni et al., 2010), and it is therefore difficult to make further comments on the accuracy of different lift force models. Clearly, however, the use of constant lift coefficient forces the choice to be made between a wall- or a core-peaked void fraction profile before any simulation. However, the present study is limited to flows exhibiting wall-peaked void fraction profiles.

A bubble depleted region characterizes the portion of a flow very close to the wall. Normally, this has been modelled using the influence of the wall lubrication force, generated by the

asymmetric flow distribution around the bubbles flowing close to a solid wall (Antal et al., 1991):

$$\mathbf{F}_w = \max\left(0, C_{w,1} + C_{w,2} \frac{d_B}{y_w}\right) \alpha \rho_c \frac{|\mathbf{U}_r|^2}{d_B} \mathbf{n}_w \quad (8)$$

In the previous equation,  $\mathbf{n}_w$  is the normal to the wall, and  $C_{w1}$  and  $C_{w2}$  modulate the strength and the region of influence of the wall force. If numerous values and models of the lift coefficient can be found in literature, even more have been proposed for  $C_{w1}$  and  $C_{w2}$ . Often, their values depend on the experimental data set being predicted and the lift force model used and, consequently, a lot of uncertainty exists. In this work, values are taken from Colombo and Fairweather (2015), where numerous bubbly flows in pipes were predicted using  $C_{w1} = -0.4$  and  $C_{w2} = 0.3$  with a  $k$ - $\varepsilon$  turbulence model, and  $C_{w1} = -0.65$  and  $C_{w2} = 0.45$  with a Reynolds stress turbulence model.

The turbulent dispersion force is modelled after Burns et al. (2004) who derived an expression by applying Favre-averaging to the drag force:

$$\mathbf{F}_{td} = \frac{3}{4} \frac{C_D \alpha \rho_c |\mathbf{U}_r|}{d_B} \frac{\nu_{t,c}}{\sigma_\alpha} \left( \frac{1}{\alpha} + \frac{1}{(1-\alpha)} \right) \nabla \alpha \quad (9)$$

Here,  $\nu_{t,c}$  is the turbulent kinematic viscosity of the continuous phase and  $\sigma_\alpha$  the turbulent Prandtl number for the volume fraction, assumed equal to 1.0.

### 3.2. Multiphase turbulence modelling

Turbulence is resolved in the continuous phase using Reynolds-averaged Navier-Stokes (RANS) turbulence models. Three models are used: a high-Reynolds number  $k$ - $\varepsilon$  model and RSM, and the EB-RSM that allows solution of the flow field up to the near-wall region.

The  $k$ - $\varepsilon$  model uses a multiphase formulation of the standard model from Jones and Launder (1972), and balance equations for the turbulence kinetic energy  $k$  and the turbulence energy dissipation rate  $\varepsilon$  are given as (CD-adapco, 2016):

$$\begin{aligned} \frac{\partial}{\partial t} ((1-\alpha) \rho_c k_c) + \frac{\partial}{\partial x_i} ((1-\alpha) \rho_c U_{i,c} k_c) \\ = \frac{\partial}{\partial x_i} \left[ (1-\alpha) \left( \mu_c + \frac{\mu_{t,c}}{\sigma_k} \right) \frac{\partial k_c}{\partial x_i} \right] + (1-\alpha) (P_{k,c} - \rho_c \varepsilon_c) \\ + (1-\alpha) S_k^{BI} \end{aligned} \quad (10)$$

$$\begin{aligned}
\frac{\partial}{\partial t}((1-\alpha)\rho_c\varepsilon_c) + \frac{\partial}{\partial x_i}((1-\alpha)\rho_c U_{i,c}\varepsilon_c) \\
= \frac{\partial}{\partial x_i} \left[ (1-\alpha) \left( \mu_c + \frac{\mu_{t,c}}{\sigma_\varepsilon} \right) \frac{\partial \varepsilon_c}{\partial x_i} \right] + (1-\alpha) \frac{\varepsilon_c}{k_c} (C_{\varepsilon,1} P_{k,c} - C_{\varepsilon,2} \rho_c \varepsilon_c) \\
+ (1-\alpha) S_\varepsilon^{BI}
\end{aligned} \quad (11)$$

In Eqs. (10) and (11),  $P_{k,c}$  is the production term due to shear and  $S_k^{BI}$  and  $S_\varepsilon^{BI}$  the source terms due to bubble-induced turbulence. The turbulent viscosity  $\mu_{t,c}$  is evaluated from the single-phase  $k$ - $\varepsilon$  formulation:

$$\mu_{t,c} = C_\mu \rho_c \frac{k_c^2}{\varepsilon_c} \quad (12)$$

Turbulence in the dispersed phase is not explicitly resolved, but it is obtained from the continuous phase turbulence field:

$$\mu_{t,d} = \frac{\rho_d}{\rho_c} C_t^2 \mu_{t,c} \quad (13)$$

with  $C_t$  assumed equal to 1. This approximation, valid for dispersed two-phase flow, is justified in view of the very low value of the density ratio in air-water flows, which causes the Reynolds stress in the gas to be much smaller than in the liquid (Gosman et al., 1992; Behzadi et al., 2004).

The bubble contribution to the turbulence is accounted for by considering the conversion of energy lost by the bubbles to drag into turbulence kinetic energy in the bubble wakes (Kataoka and Serizawa, 1989; Troshko and Hassan, 2001; Rzehak and Krepper, 2013). The turbulence kinetic energy equation source term  $S_k^{BI}$  is expressed as:

$$S_k^{BI} = K_{BI} \mathbf{F}_d \mathbf{U}_r \quad (14)$$

$\mathbf{F}_d$  is the drag force and  $K_{BI}$  is introduced to account for the modulation of the turbulence source. In the turbulence energy dissipation rate equation, the bubble-induced source is expressed as the corresponding turbulence kinetic energy source term, but multiplied by the timescale of the bubble-induced turbulence  $\tau_{BI}$ :

$$S_\varepsilon^{BI} = \frac{C_{\varepsilon,BI}}{\tau_{BI}} S_k^{BI} \quad (15)$$

In shear-induced single-phase turbulence modelling, the turbulence timescale corresponds to the lifetime of a turbulent eddy before it breaks up into smaller structures. In multiphase turbulence, the situation is more complex and the bubble-induced turbulence timescale should also be related to the bubble length and velocity scales. At the present time, a generally accepted formulation is yet to emerge. In this work, the recent proposal of a mixed timescale from Rzehak and Krepper (2013) is adopted. Consequently, the velocity scale is derived from the square root of the liquid turbulence kinetic energy and the length scale from the bubble diameter. In addition, a value of  $K_{BI} = 0.25$  is used in Eq. (14), this value having been arrived at through optimization by Colombo and Fairweather (2015) when predicting a large database of bubbly flows.

The multiphase Reynolds stress turbulence model formulation adopted is based on the single-phase transport equations of the Reynolds stresses,  $R_{ij} = \tau_{ij}^{Re} / \rho_c$  (CD-adapco, 2016):

$$\begin{aligned} \frac{\partial}{\partial t} \left( (1 - \alpha) \rho_c R_{ij} \right) + \frac{\partial}{\partial x_j} \left( (1 - \alpha) \rho_c U_{i,c} R_{ij} \right) \\ = \frac{\partial}{\partial x_j} \left[ (1 - \alpha) D_{R,ij} \right] + (1 - \alpha) (P_{ij} + \rho_c \Phi_{ij} - \rho_c \varepsilon_{ij}) + (1 - \alpha) S_{ij}^{BI} \end{aligned} \quad (16)$$

Here,  $P_{ij}$  is the turbulence production. The Reynolds stress diffusion  $D_{R,ij}$  is modelled accordingly to Daly and Harlow (1970), whilst the isotropic hypothesis is used for the turbulence dissipation rate term  $\varepsilon_{ij}$ .  $\Phi_{ij}$  is the pressure-strain model accounting for pressure fluctuations that redistribute the turbulence energy amongst the various Reynolds stress components. The pressure-strain relation is modelled using the so-called ‘‘SSG model’’ (Speziale et al., 1991), which is quadratically non-linear in the turbulence anisotropy tensor:

$$\begin{aligned} \Phi_{ij}^h = -[C_{1a}\varepsilon + C_{1b}tr(P)]a_{ij} + C_2\varepsilon \left( a_{ik}a_{kj} - \frac{1}{3}a_{mn}a_{mn}\delta_{ij} \right) \\ + \left[ C_{3a} - C_{3b}(a_{ij}a_{ij})^{0.5} \right] kS_{ij} \\ + C_4k \left( a_{ik}S_{jk} + a_{jk}S_{ik} - \frac{2}{3}a_{mn}S_{mn}\delta_{ij} \right) + C_5(a_{ik}W_{jk} + a_{jk}W_{ik}) \end{aligned} \quad (17)$$

Here,  $a_{ij}$  are components of the anisotropy tensor, and  $S_{ij}$  and  $W_{ij}$  are the strain rate and the rotation rate tensors, respectively. The bubble-induced turbulence source term is calculated using Eq. (14). The source is then split amongst the normal Reynolds stress components according to Colombo and Fairweather (2015), who apportion a higher fraction of the bubble-induced turbulence source to the streamwise direction (Lopez de Bertodano et al., 1990):

$$S_{ij}^{BI} = \begin{bmatrix} 1.0 & 0.0 & 0.0 \\ 0.0 & 0.5 & 0.0 \\ 0.0 & 0.0 & 0.5 \end{bmatrix} S_k^{BI} \quad (18)$$

A high Reynolds number wall treatment, where the velocity in the first near-wall computational cell is imposed from the single-phase law of the wall, is used with both the  $k$ - $\varepsilon$  model and the RSM. The EB-RSM (Manceau and Hanjalic, 2002; Manceau, 2015), in contrast, blends the quasi-homogeneous SSG model from Eqs. (16) and (17) with a near-wall formulation that reproduces the correct asymptotic behaviour of the turbulent stresses near the wall. In the vicinity of a wall the turbulence field is strongly anisotropic and the impermeability requirement at the wall exerts a kinematic blockage effect on the wall-normal velocity fluctuations. At the same time, the wall reflects pressure fluctuations, the so-called wall echo effect, which, in opposition to wall blockage, favours the redistribution of energy to the wall-normal component of the turbulence. The correct asymptotic behaviour of the pressure-strain relation near a wall is modelled using the following relation:

$$\Phi_{ij}^w = -5 \frac{\varepsilon}{k} \left[ \overline{u_i u_k} n_j n_k + \overline{u_j u_k} n_i n_k - \frac{1}{2} \overline{u_k u_l} n_k n_l (n_i n_j + \delta_{ij}) \right] \quad (19)$$

In the previous equation,  $n$  are the components of the wall-normal vector. Transition from the near-wall model in Eq. (19) to the weakly inhomogeneous behaviour away from the wall is ensured by the elliptic relaxation function  $\alpha_{EB}$ :

$$\Phi_{ij} = (1 - \alpha_{EB}^3) \Phi_{ij}^w + \alpha_{EB}^3 \Phi_{ij}^h \quad (20)$$

The elliptic relaxation function is obtained by solving the following elliptic relaxation equation with the  $\alpha_{EB} = 0$  wall boundary condition:

$$\alpha_{EB} - L_t \nabla^2 \alpha_{EB} = 1 \quad (21)$$

The turbulent length scale  $L_t$  then follows from:

$$L_t = C_l \max \left( C_\eta \frac{v^{3/4}}{\varepsilon^{1/4}}, \frac{k^{3/2}}{\varepsilon} \right) \quad (22)$$

Similarly, the near-wall behaviour of the turbulence energy dissipation rate is imposed using the elliptic relaxation function:

$$\varepsilon_{ij} = (1 - \alpha_{EB}^3) \frac{\overline{u_i u_j}}{k} \varepsilon + \frac{2}{3} \alpha_{EB}^3 \varepsilon \delta_{ij} \quad (23)$$

At the wall, the following boundary condition is used for the turbulence energy dissipation rate:

$$\varepsilon = 2\nu \lim_{y_w \rightarrow 0} \frac{k}{y_w^2} \quad (24)$$

Values of all the model coefficients used can be found in Table 2. The model for the bubble-induced contribution to the continuous phase turbulence (Eqs. (14) and (15)) has been implemented in the EB-RSM, this being vital to obtaining accurate predictions of the turbulence intensity in bubbly flows (Colombo and Fairweather, 2015). The bubble-induced contribution is partitioned among the normal turbulent stress components using Eq. (18).

A summary of the turbulence and interfacial closures used in the different models is provided in Table 3, together with the experiments predicted with each model.

Table 2. Coefficients used in the various turbulence models.

$C_\mu$	$C_{\varepsilon,1}$	$C_{\varepsilon,2}$	$\sigma_k$	$\sigma_\varepsilon$	$K_{BI}$	$C_{\varepsilon,BI}$	$C_{1a}$
0.09	1.44	1.92	1.0	1.3	0.25	1.0	1.7
$C_{1b}$	$C_2$	$C_{3a}$	$C_{3b}$	$C_4$	$C_5$	$C_l$	$C_\eta$
0.9	1.05	0.8	0.65	0.625	0.2	0.133	80

Table 3. Summary of the model settings and experiments predicted.

	<b>EB-RSM</b>	<b>RSM</b>	<b><math>k - \varepsilon</math></b>	<b><math>k - \varepsilon</math> Tomiyama</b>
<b>Turbulence</b>	SSG RSM (Speziale et al., 1991). Elliptic Blending near-wall treatment	SSG RSM (Speziale et al. 1991). High-Reynolds number wall treatment	$k - \varepsilon$ (Jones and Launder, 1972). High-Reynolds number wall treatment	$k - \varepsilon$ (Jones and Launder, 1972). High-Reynolds number wall treatment
<b>Bubble-induced turbulence</b>	Colombo and Fairweather (2015)	Colombo and Fairweather (2015)	Colombo and Fairweather (2015)	Colombo and Fairweather (2015)
<b>Drag</b>	Tomiyama et al. (2002a)	Tomiyama et al. (2002a)	Tomiyama et al. (2002a)	Tomiyama et al. (2002a)
<b>Lift</b>	Neglected	Constant coefficient. $C_L = 0.1$	Constant coefficient. $C_L = 0.1$	Tomiyama et al. (2002b)
<b>Wall Lubrication</b>	Neglected	Antal et al. (1991). $C_{w1} = -0.4$ $C_{w2} = 0.3$	Antal et al. (1991). $C_{w1} = -0.65$ $C_{w2} = 0.45$	Antal et al. (1991). $C_{w1} = -0.4$ $C_{w2} = 0.3$
<b>Turbulent Dispersion</b>	Burns et al. (2004)	Burns et al. (2004)	Burns et al. (2004)	Burns et al. (2004)
<b>Experiments*</b>	HT, LB, Sun, Hos	HT, LB, Sun, Hos	HT, LB, Sun, Hos	HT, LB

\*In relation to Table 1: HT: Hosokawa and Tomiyama (2009); LB: Liu and Bankoff (1993a); Sun: Sun et al. (2014); Hosokawa et al. (2014).

### 3.3. Numerical settings

Numerical simulations were performed using the STARCCM+ code (CD-adapco, 2016). Pipe flows were simulated in a two-dimensional axisymmetric geometry, whereas 1/4 sections were used for both the square duct and the rod bundles. Constant inlet phase velocity and void fraction boundary conditions were imposed. Pressure was fixed on the outlet section. Flow conditions were fully-developed and a zero gradient condition was imposed on all other flow quantities. The no-slip boundary condition was imposed at the wall. For the high-Reynolds number wall treatment, velocity in the near-wall cell was imposed from the single-phase law of the wall. For the EB-RSM model, the velocity field was finely resolved in the near-wall region. Turbulence in this region was handled by modelling the asymptotic behaviour of the pressure-strain relation and the turbulence dissipation rate using the elliptic blending approach (Section 3.2). At the wall, zero values of the turbulent stresses were imposed. For the turbulence dissipation rate, the limit  $\varepsilon = 2\nu(k/y_w)_{y_w \rightarrow 0}$  was imposed.

Uniform profiles of water and vapour velocity, and the void fraction, were obtained from superficial velocities (Table 1) from the experiments and imposed at the inlet section. A small amount of turbulence (intensity  $\sim 1\%$ ) was also imposed. The same values of velocity, void



fraction and turbulence intensity were used for the initial condition. Results were recorded at a sufficient distance from the inlet to ensure the flow had reached fully-developed conditions and any influence of the inlet conditions had disappeared. Detailed measurements of the bubble diameter distribution at different heights after bubble injection are a rarity in the literature and no measurements of this kind are available for the experiments considered. However, experiments were selected from mono-dispersed bubble size distribution tests that can be characterized reasonably-well with a single average bubble diameter. In addition the bubble diameter in the simulations was fixed using averaged values or local lateral profiles that were available at the measurement plane for all 4 experiments. This, in conjunction with the mono-dispersed size distribution, ensured that simulations were representative of local experimental conditions at the measurement plane, even without accounting for break up and coalescence through, for example, a population balance equation. Specifically, the bubble diameter was set to  $d_B = 3.66$  mm for Hosokawa and Tomiyama (2009) and  $d_B = 3.0$  mm for Liu and Bankoff (1993a), based on the bubble diameter distributions available. Values for Sun et al. (2014) and Hosokawa et al. (2014) were obtained from averaging the lateral profile at the measurement plane. These profiles show an almost constant average bubble diameter across the cross-section, with values  $d_B = 4.25$  mm for Sun et al. (2014) and  $d_B = 3.0$  mm for Hosokawa et al. (2014). For Sun et al. (2014) the value is slightly higher and approaches the transition region where the behaviour of the bubbles (and the direction of the lift force) change, driven by the deformation of their shape. However, wall-peaked void fraction profiles from the experiment reasonably suggest that the bubbles still preferentially accumulate towards the wall and the mono-dispersed approximation (and a positive lift coefficient) still holds. Using CFD results, values of the bubble Reynolds, Eötvös and Morton numbers have been calculated and are reported in Table 4. The Reynolds number range is representative of bubbles in the wall region (low value) and in the centre of the duct (high value). According to the classification of Clift et al. (1978), the bubble shape is on the boundary between spherical (at the wall) and slightly deformed-ellipsoidal bubbles (in the centre). Even in the centre, however, deformation does not approach the cap-bubble shape that determines the change of bubble behaviour (accumulation in the centre driven by the lift force).

Table 4. Bubble characteristics in the four experiments

Experiment	$d_B$ [m]	$Re_B$ [-]	$Eo$ [-]	$Mo$ [-]
Hosokawa and Tomiyama (2009)	0.00366	300-675	1.8	$1.36 \cdot 10^{-13}$
Liu and Bankoff (1993a)	0.003	130-640	1.21	$1.36 \cdot 10^{-13}$
Sun et al. (2014)	0.00425	545-1120	2.42	$3.623 \cdot 10^{-14}$
Hosokawa et al. (2014)	0.003	330-650	1.21	$8.48 \cdot 10^{-14}$

Pressure-velocity coupling was solved using a multiphase extension of the SIMPLE algorithm and second-order upwind schemes were used to discretize the velocity, volume fraction, turbulent stresses, turbulence kinetic energy and dissipation rate convective terms. Under-relaxation factors of 0.5 for the momentum equations, 0.4 for the pressure, 0.25 for the void fraction and 0.6 for the turbulence were found sufficient to ensure a smooth convergence of the results. Simulations were advanced in time with a second-order implicit scheme. The Courant number was kept under a maximum value of 2 and, after an inlet development region, fully developed steady-state conditions were reached before recording the results. Strict convergence of residuals (pressure, velocity, volume fraction and turbulence quantities) was ensured ( $< 10^{-5}$ ) and the mass balance was checked to have an error always less than 0.1 % for both phases.

Structured meshes were employed and sensitivity studies were made to ensure mesh-independent solutions. For the high Reynolds number turbulence models, care was taken to ensure the first near-wall grid point was always located at a non-dimensional distance from the wall  $y^+$  greater than 30, in the region of validity of the law of the wall. In contrast, the EB-RSM model requires a much more refined mesh in the near-wall region. In this region, solutions of the transport equations away from the wall are blended with a near-wall model for the turbulence stresses and the turbulence energy dissipation rate. Results of the mesh sensitivity study are reported in detail for the Hosokawa and Tomiyama (2009) pipe flow experiment. Three different meshes were tested, with the number of elements equal to  $20 \times 500$ ,  $26 \times 800$  and  $40 \times 1500$ . Radial profiles of the water mean velocity, void fraction, radial turbulent stress and Reynolds shear stress are provided in Figure 1. The void fraction and velocity profiles do not show any meaningful differences between the three meshes considered. For the turbulence parameters, the solution changes from the least-refined to the medium grid, with additional refinement then showing no significant changes in the radial profiles given in Figure 1. Consequently, the medium mesh (20,800 cells) was selected for the simulations employing the EB-RSM. Similar studies were made for the Liu and Bankoff (1993a), Sun et al. (2014) and Hosokawa et al. (2014) experiments, and mesh-independent solutions were obtained using 44,800 (in two-dimensional axisymmetry), 1,280,000 and 369,600 cells, respectively. In all the meshes, the centre of the near-wall cell was located at a wall distance  $y^+$  in the range 1 – 1.5, sufficient for the application of the elliptic blending modelling strategy. Corresponding meshes for the high Reynolds models employed 3,750, 129,375 and 146,825 cells, with 3000 used for the experiment of Hosokawa and Tomiyama (2009).

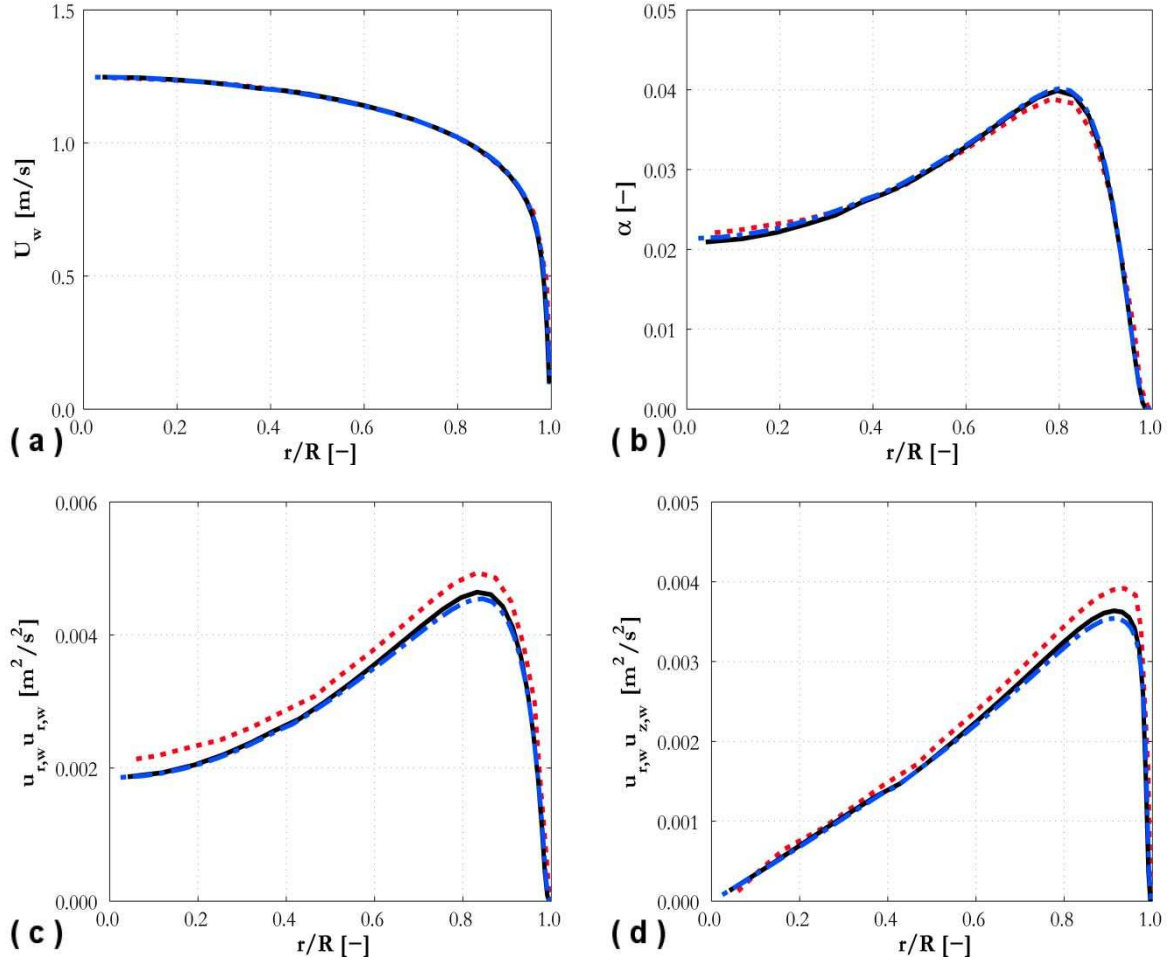


Figure 1. Mesh sensitivity study for the Hosokawa and Tomiyama (2009) experiment: (a) water mean velocity; (b) air void fraction; (c) radial turbulent stress; and (d) Reynolds shear stress (---  $175 \times 500$ ; —  $276 \times 800$ ; - - -  $700 \times 1500$ ).

## 4. Results and discussion

### 4.1. Pipe flows

The Hosokawa and Tomiyama (2009) experiment was simulated first with the EB-RSM and the predicted void fraction profile is shown in Figure 2. Interestingly, the wall-peaked void profile that characterizes bubbly flows in pipes is clearly visible, even if the lift force and wall lubrication are neglected. Although, the value of the peak is underestimated and too high values of the void fraction are predicted in the centre of the pipe. At steady-state, and in the absence of lift and wall forces, in a pipe the momentum balance in the radial direction for the liquid and the gas phase reduces to:

$$\frac{\alpha_l \partial p}{\rho_l \partial r} = \frac{F_{td,r}}{\rho_l} - \frac{\partial \alpha_l \overline{u_r u_r^l}}{\partial r} + \frac{\alpha_l}{r} (\overline{u_\theta u_\theta^l} - \overline{u_r u_r^l}) \quad (25)$$

$$\frac{\alpha_g}{\rho_g} \frac{\partial p}{\partial r} = -\frac{F_{td,r}}{\rho_g} - \frac{\partial \alpha_g \overline{u_r u_r^g}}{\partial r} + \frac{\alpha_g}{r} (\overline{u_\theta u_\theta^g} - \overline{u_r u_r^g}) \quad (26)$$

As anticipated in Ullrich et al. (2014), the pressure gradient can be eliminated to obtain an equation for the radial void fraction distribution:

$$\begin{aligned} \frac{\partial \alpha_g}{\partial r} \left[ \frac{\rho_g}{\alpha_g} \overline{u_r u_r^g} + \frac{\rho_l}{\alpha_l} \overline{u_r u_r^l} \right] \\ = -\frac{F_{td,r}}{\alpha_g} - \frac{F_{td,r}}{\alpha_l} - \rho_g \frac{\partial \overline{u_r u_r^g}}{\partial r} + \rho_l \frac{\partial \overline{u_r u_r^l}}{\partial r} \\ + \frac{\rho_g}{r} (\overline{u_\theta u_\theta^g} - \overline{u_r u_r^g}) - \frac{\rho_l}{r} (\overline{u_\theta u_\theta^l} - \overline{u_r u_r^l}) \end{aligned} \quad (27)$$

Turbulence quantities are proportional to the phase density. In gas-liquid bubbly flows, where the density ratio  $\rho_g / \rho_l$  can be as low as  $10^{-3}$ , the turbulence stresses in the gas phase can be neglected. Rearranging, the following equation can be obtained:

$$\alpha_g \frac{\partial \alpha_g}{\partial r} = -\frac{F_{td,r}}{\rho_l \overline{u_r u_r^l}} + \frac{\alpha_g (1 - \alpha_g)}{\overline{u_r u_r^l}} \left[ \frac{\partial \overline{u_r u_r^l}}{\partial r} + \left( \frac{\overline{u_r u_r^l} - \overline{u_\theta u_\theta^l}}{r} \right) \right] \quad (28)$$

Clearly, from Eq. (28), turbulence in the liquid phase strongly impacts the phase distribution and is responsible for the preferential accumulation of bubbles near the wall in Figure 2 in the absence of lift and wall forces, with turbulent dispersion from Eq. (9) working against flow property gradients. More specifically, because of the very low density of the bubbles, the inertia of the bubbles is negligible with respect to the inertia of the fluid and turbophoresis is not sufficient to explain the wall-peaked void fraction profile. This is in contrast to solid particle flows, where the density of the dispersed phase is at least comparable and often higher than that of the carrier phase, such that the inertia of the particles and turbophoresis have a much more important impact on particle preferential distribution.

In gas-liquid bubbly flows, from Eq. (25) the continuous phase turbulence, and in particular the gradient in the radial turbulent stress, generates a radial pressure gradient in the flow. This pressure gradient pushes the bubbles towards the lower pressure region near the wall. There, pressure reaches a minimum and the subsequent increase as the wall is approached prevents the bubbles reaching the very near-wall region, shaping the wall-peaked void fraction profile of Figure 2. This effect is clearly visible in Figure 3, where the radial profile of the radial turbulent normal stress and the pressure are shown. Between the right-hand side terms in Eq.

(28), the first and second are dominant and comparable. Most importantly, a detailed specification of the void fraction profile near the wall needs the turbulence field in that region to be finely resolved. To do so, a turbulence model able to resolve the flow field down to the viscous sub-layer is necessary. When this is the case, the peak in the void fraction distribution can be predicted, as well as the subsequent decrease to zero towards the wall, even when neglecting any repulsive force such as wall lubrication. These results are compared against predictions of the high-Re turbulence models in Figure 4. Good accuracy is obtained using the  $k-\varepsilon$  and RSM models for the liquid mean velocity profile (Figure 4a). Distinctive features of the void fraction profile (Figure 4b) are well-reproduced by all the models, although the high-Re RSM is more accurate. However, the results obtained from the EB-RSM model suggest that the impact of turbulence on the phase distribution is at least as significant as lift and wall lubrication. Although radial changes in the pressure values are not dramatic (Figure 3b), the small radial distance results in a significant contribution from the pressure gradient term in Eq. (2). Its impact is comparable to that of the lift force (from high Reynolds number simulations) away from the wall and reaches values as high as  $50 \text{ N m}^{-3}$  near the wall. In the near-wall region itself, the pressure gradient contribution is significant when compared to that of the lift and wall forces, which was observed to reach  $80\text{-}90 \text{ N m}^{-3}$ . It is, however, worth mentioning that quantitative values of the lift and wall forces are unavoidably strongly coupled with each other and arbitrarily related to the coefficients used in the respective models. It is possible that the same void profile would have been obtained by reducing the contribution from both forces by a similar amount.

Comparison of the void fraction profiles from the high-Re  $k-\varepsilon$  and RSM in Figure 4b confirms the role of the pressure gradient. The impact of the lift force is similar between the two models. However, the RSM model correctly predicts the radial pressure gradient, at least away from the near-wall region, and shows a higher and more accurate peak. This suggests the EB-RSM model can still be improved with the addition of a proper lift force contribution, which will be investigated in the last section of this paper. Thanks to the resolution in the near-wall region, however, the wall lubrication contribution required by the high-Re models seems unnecessary with the EB-RSM model.

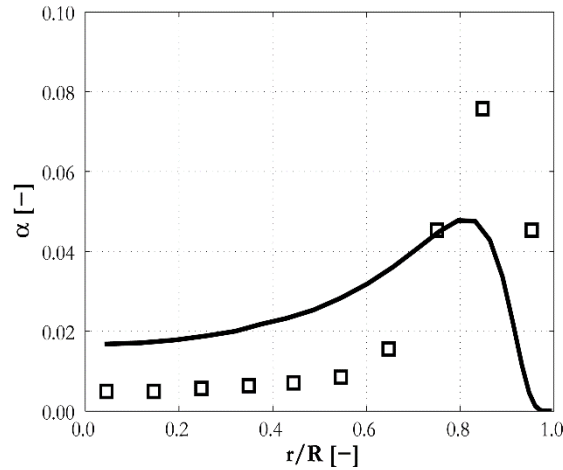


Figure 2. Radial void fraction profile using the EB-RSM model compared against the Hosokawa and Tomiyama (2009) experiment ( $\square$  data; — EB-RSM).

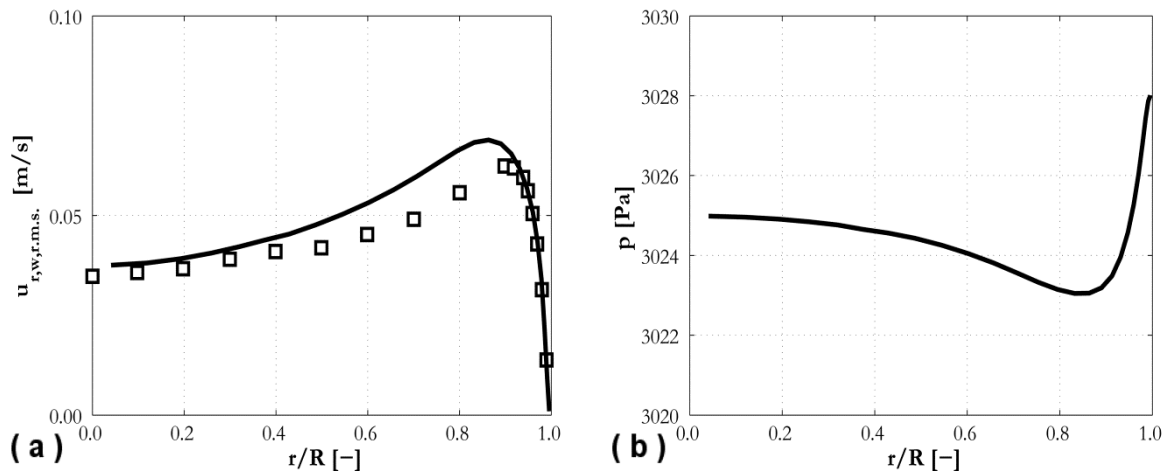


Figure 3. Radial variation of (a) r.m.s. of turbulent radial velocity fluctuations in water and (b) pressure using the EB-RSM model compared against the Hosokawa and Tomiyama (2009) experiment ( $\square$  data; — EB-RSM).

The near-wall capabilities of the EB-RSM are also shown in the accurate prediction of the peak in the turbulence kinetic energy near the wall in Figure 4c. Turbulence levels are well-predicted by including the contribution to turbulence from the bubbles. Anisotropy of the turbulence field and the behaviour of the turbulent stresses close to the wall are also well-predicted by the EB-RSM in Figure 4d, where radial profiles of the r.m.s. (root-mean-square) of the velocity fluctuations are compared against data from the Hosokawa and Tomiyama (2009) experiment. Good agreement is obtained, except for an overestimation of the azimuthal fluctuations in the near-wall region.

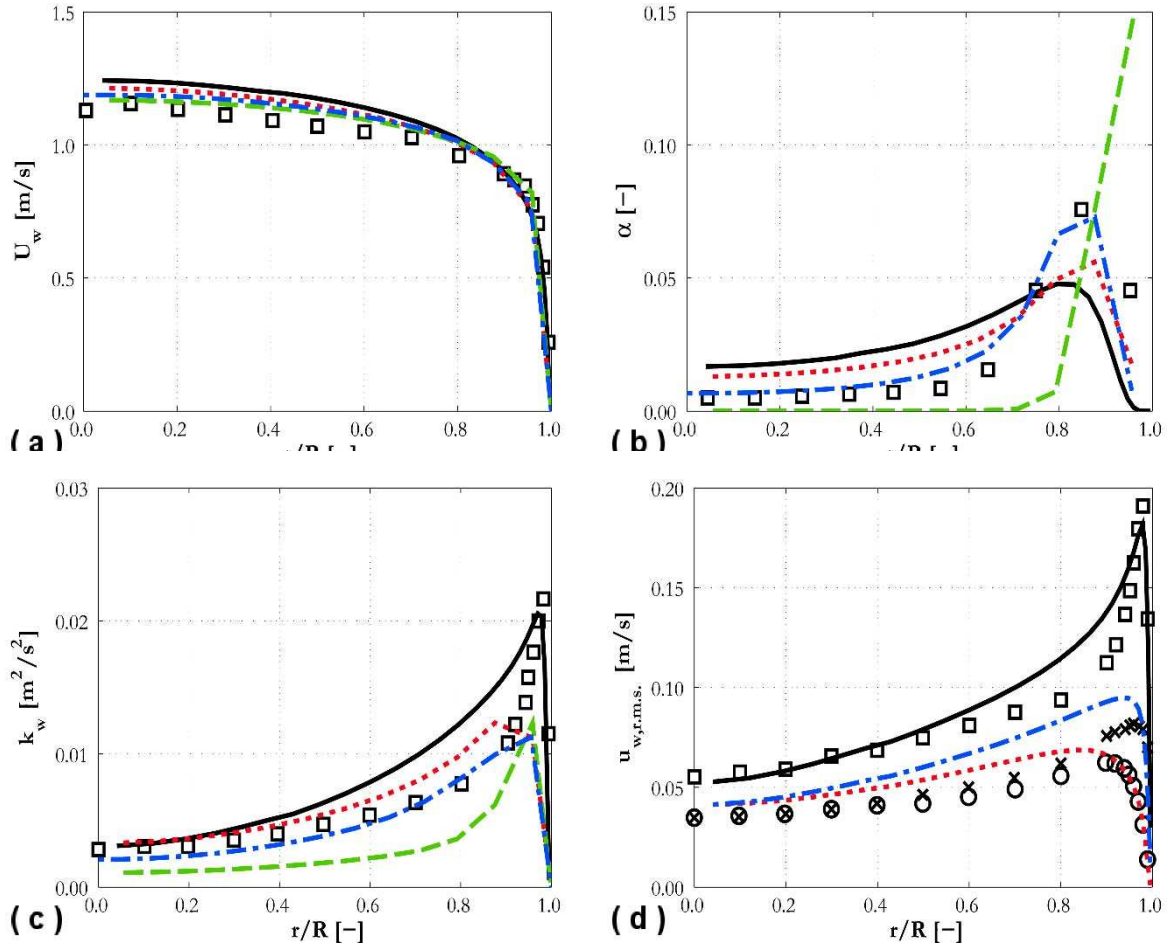


Figure 4. Radial predictions of (a) water mean axial velocity, (b) void fraction, (c) water turbulence kinetic energy and (d) r.m.s. of water velocity fluctuations compared against the Hosokawa and Tomiyama (2009) experiment (In (a)-(c):  $\square$  data; — EB-RSM; - - - RSM; ---  $k - \varepsilon$ ; - -  $k - \varepsilon$  with Tomiyama lift. In (d): EB-RSM predictions against data in:  $\square$ , — axial direction;  $\circ$ , --- radial direction;  $\times$ , - - - azimuthal direction).

In Figure 4,  $k-\varepsilon$  results are shown for both a constant lift coefficient and the Tomiyama et al. (2002b) correlation. The constant lift model provides satisfactory accuracy, in line with experiments and other model predictions. In contrast, the Tomiyama et al. (2002b) correlation predicts too high a void fraction peak near the wall that rapidly diminishes to negligible values towards the centre of the pipe. The contribution of bubbles to the continuous phase turbulence in the latter region is therefore absent and, consequently, turbulence kinetic energy is under predicted. These findings confirm similar results reported in Colombo and Fairweather (2015). Therefore, and despite the relatively higher accuracy found for the other pipe flow experiment presented below, the Tomiyama et al. (2002b) model has not been used with the RSM, and in the following simulations with the  $k-\varepsilon$  model.

The Hosokawa and Tomiyama (2009) experiment was carried out at relatively low void fraction. Therefore, comparisons were extended to a higher void fraction pipe flow using the experiment data from Liu and Bankoff (1993a), with comparisons reported in Figure 5. Good predictions of the peak in the void fraction are obtained with all the models considered. However, in the centre of the pipe, the EB-RSM predicts a wavy behaviour in the void fraction instead of the flat profile obtained with the alternative approaches. Although not completely flat, the experimental data confirm the high Reynolds number results. An increase in the liquid mean velocity towards the centre of the pipe predicted by the EB-RSM reflects the similar increase in the void fraction, whilst the other models again predict a flat velocity profile. Unfortunately, no experimental data on the liquid mean velocity are available for this experiment. Although the behaviour towards the centre of the pipe is not well-predicted by the EB-RSM, the qualitative features of a wall-peaked void fraction profile are again obtained without considering the lift and wall lubrication contributions. As noted, better results are shown by the other models in regards to the void fraction towards the centre of the pipe, including that based on the Tomiyama et al. (2002b) approach, although the near-wall peak obtained using the latter is not in agreement with the data. As already mentioned, because of inconsistencies in the results obtained with the Tomiyama et al. (2002b) model, it was not used with the RSM or in all other following simulations using the  $k-\varepsilon$  turbulence model.

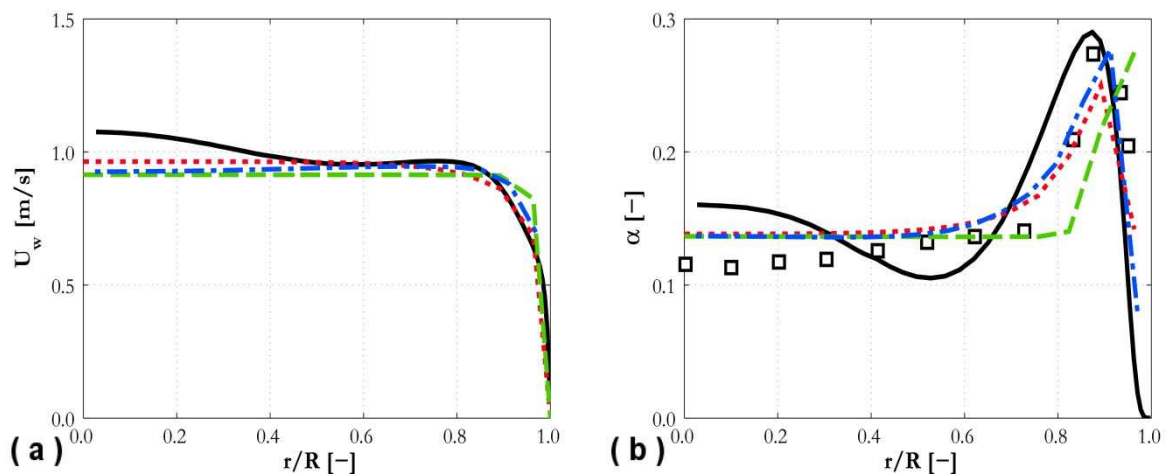


Figure 5. Radial predictions of (a) water mean axial velocity and (b) void fraction compared against the Liu and Bankoff (1993a) experiment ( $\square$  data; — EB-RSM; - - - RSM; ---  $k-\varepsilon$ ; - -  $k-\varepsilon$  with Tomiyama lift).

Turbulence generates a radial pressure gradient (Figure 6), similar to that observed in the Hosokawa and Tomiyama experiment (2009), which is responsible for the bubble preferential



accumulation. Comparisons between data and EB-RSM predictions for the radial profiles of the streamwise and radial r.m.s. of the velocity fluctuations are also given in this figure. Although turbulence anisotropy is predicted, the accuracy is not as high as for the low void fraction case (Figure 4). More specifically, the streamwise turbulent fluctuations are under predicted in the centre of the pipe and over predicted in the near-wall region. For comparison, the high-Re RSM predictions are also included in Figure 6a. Similar discrepancies are found, although the high-Re RSM also under predicts the streamwise r.m.s. in the near-wall region. The radial pressure profile shows a low-pressure region near the wall, with the pressure initially increasing but then slightly decreasing again in moving towards the pipe centre. This decrease promotes void fraction accumulation near the pipe centre. It is difficult to assess whether this occurs due to the absence of other momentum transfer terms, such as those due to lift and wall forces, or to inaccuracies in the prediction of the turbulence field. The effect on the oscillating behaviour of the addition of other radial forces such as lift is investigated further below.

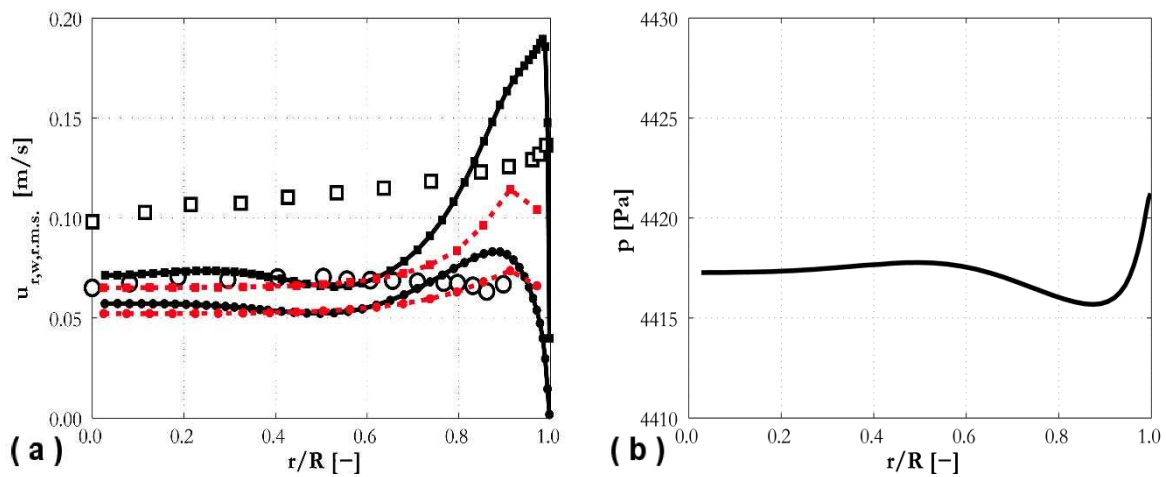


Figure 6. Radial predictions of (a) r.m.s. of turbulent radial velocity fluctuations in water and (b) pressure compared against the Liu and Bankoff (1993a) experiment (In (a):  $\square$  axial direction;  $\circ$  radial direction; — EB-RSM; --- RSM ).

#### 4.2. Square duct

Previous research has mostly focused on pipe flows, and it is therefore interesting to extend the present analysis to other geometrical configurations, such as the square duct flow studied experimentally by Sun et al. (2014). Cross-sectional views of the pressure and void fraction distribution predicted by the EB-RSM are given in Figure 7, which shows a 1/4 cross-sectional view of the square duct. Similarly to what occurs in pipes, the pressure is lower in the near-wall region with respect to the centre of the duct. The pressure is at a minimum in the corner

of the duct. Driven by the pressure, the void fraction peaks along the two lateral walls and has a distinctive maximum in the corner.

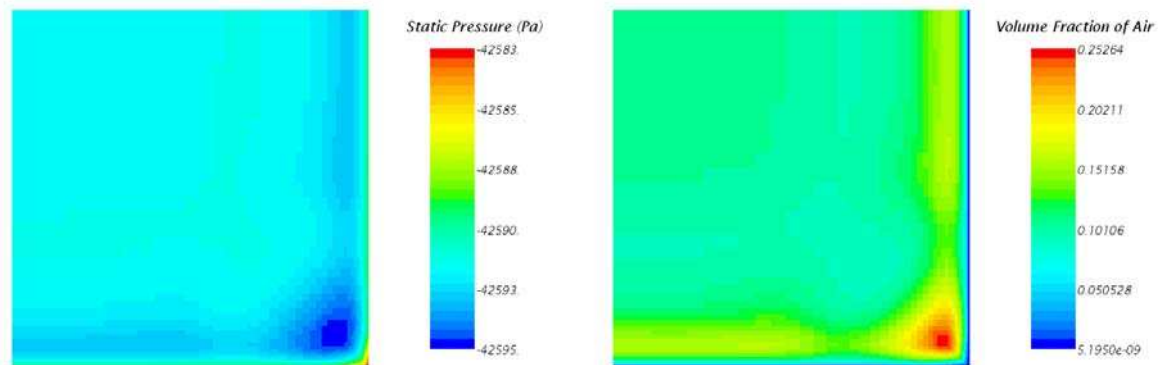


Figure 7. Pressure (left) and void fraction (right) in the square duct cross-section calculated using the EB-RSM model.

Void fraction (and pressure) distributions in the near-wall region are predicted in great detail due to the fine resolution near the walls allowed by the EB-RSM. Comparison of predictions with experimental data is given in Figure 8 for data gathered on the duct diagonal and on a line parallel to the duct wall (in the plots, results are presented as a function of the distance from the centre line along the diagonal  $d$  normalized by the diagonal half-length  $D$ , and the distance from the centre on a line parallel to the wall  $x$  normalized by the duct side half-length  $L$ ). Predictions of the RSM and  $k-\varepsilon$  models are also included. Velocity and void fraction profiles from the EB-RSM show the same wavy behaviour already noted above, with an increase in the void fraction and, consequently, of the liquid mean velocity occurring towards the centre of the duct. In contrast, the RSM and  $k-\varepsilon$  based model predictions show a flat mean velocity profile away from the duct walls, and a wall-peaked void profile that becomes flat towards the duct centre. Agreement with experiment is good using the same lift and wall force models employed for the pipe flows considered earlier. The EB-RSM predicts the near-wall peak in the velocity profiles, unlike the other models, and the peaks in the void fraction profiles with reasonable accuracy. On the duct diagonal, the EB-RSM is also the only model to predict the slight decrease in void fraction after the near-wall peak and the subsequent increase towards the centre of the duct. However, the drop in velocity and void fraction after the peaks is generally over predicted, and in some cases not supported by experimental evidence. The EB-RSM also predicts excessive turbulence kinetic energy near the duct wall but, in the centre of the duct, agreement with data is comparable to that of the other models on the diagonal and significantly improved parallel to the wall. Overall, all the models demonstrate a reasonable accuracy.

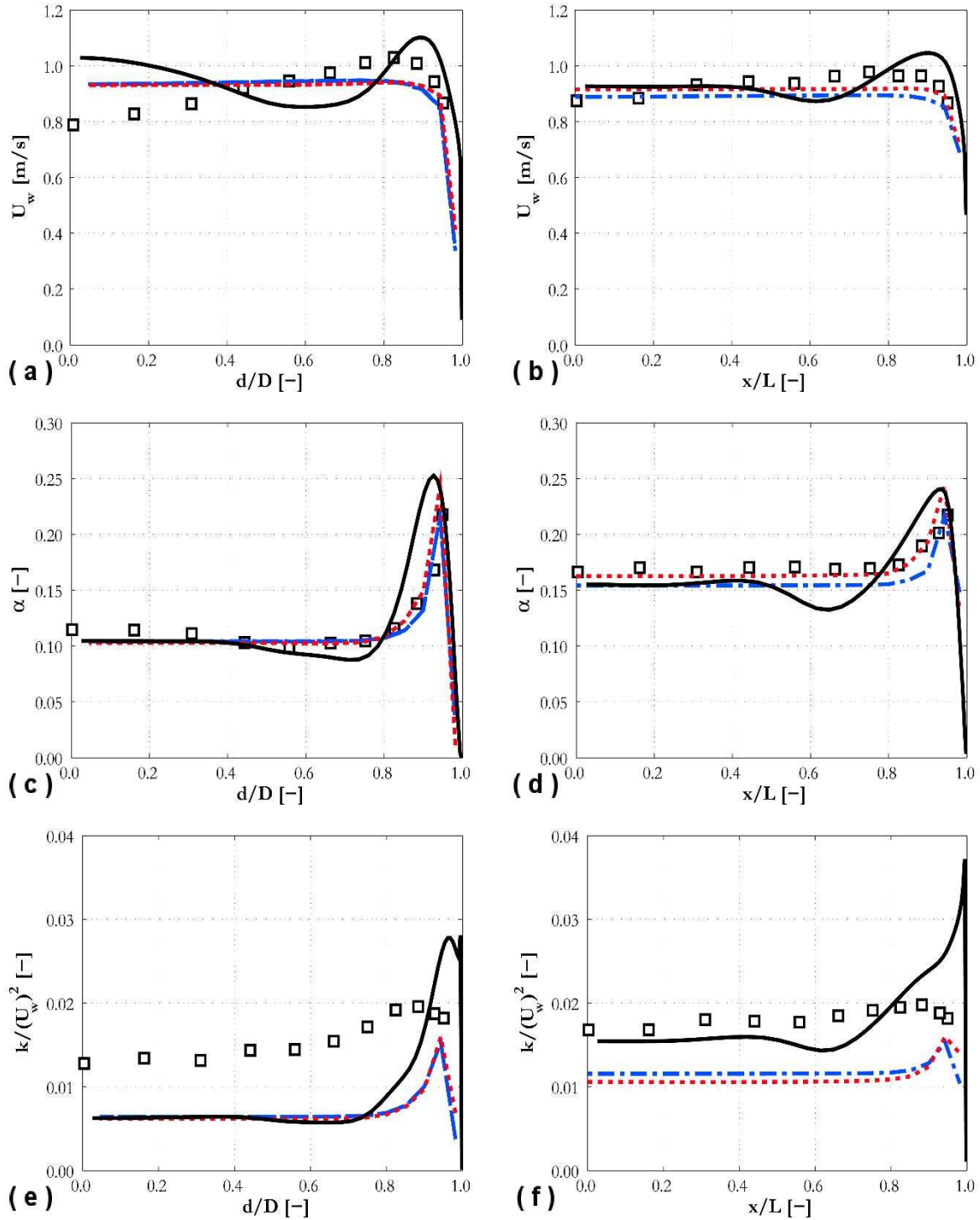


Figure 8. Predictions of (a, b) water mean axial velocity, (c, d) void fraction and (e, f) turbulence kinetic energy compared against the Sun et al. (2014) experiment. Profiles are shown on the diagonal (a, c and e, where  $d$  is the distance from the centre line along the diagonal and  $D$  the diagonal half-length) and on a line parallel to the wall (b, d and f, where  $x$  is the distance along a line from the central plane perpendicular to the line and  $L$  the duct half side length) ( $\square$  data; — EB-RSM; - - - RSM; ---  $k - \epsilon$ ).

The results in Figure 8 demonstrate how distinctive features of the flow in a square duct can be reproduced, even when lift and wall lubrication forces are neglected. Discrepancies are

observed towards the centre of the duct, with a wavy behaviour of the void fraction and velocity profiles that was also observed in the pipe flow of Liu and Bankoff (1993a). As noted earlier, the presence of additional interfacial forces such as lift may smooth out this wavy behaviour. It is worth mentioning that the aim at this stage is not to prove that the pressure gradient is the only determinant of the radial void fraction distribution, because the lift force also plays a major role. However, the impact of the multiphase turbulence field and the induced pressure field are comparable and need to be properly accounted for to permit accurate modelling. An additional interesting aspect is depicted in Figure 9, which shows flow recirculation in the same quarter of the duct cross-section used in Figure 8. Recirculation is presented as a percentage of the ratio between the cross-sectional velocity magnitude and the streamwise velocity. It is well-known how the anisotropy of the turbulence field in ducts generates recirculation zones in single-phase flows (Brundrett, 1964; Sun et al., 2014), with two counter-rotating vortices in each duct corner. This recirculation is normally well-predicted in single-phase flow by using Reynolds stress turbulence models. Corner recirculation, which amounts to around 2% of the mean streamwise velocity, is predicted by the EB-RSM model. In the left hand side of Figure 9, recirculation is clearly visible in the lower right corner of the figure that identifies the corner in the 1/4 duct cross-section. However, in the same cross-section, recirculation is not predicted by the high-Re RSM that includes lift and wall lubrication forces (right hand side of Figure 9). Even though observations in single-phase flows support the presence of a recirculation pattern, unfortunately no measurements are available for two-phase bubbly flows and additional experimental work on such flows is therefore necessary to further elucidate this specific topic.

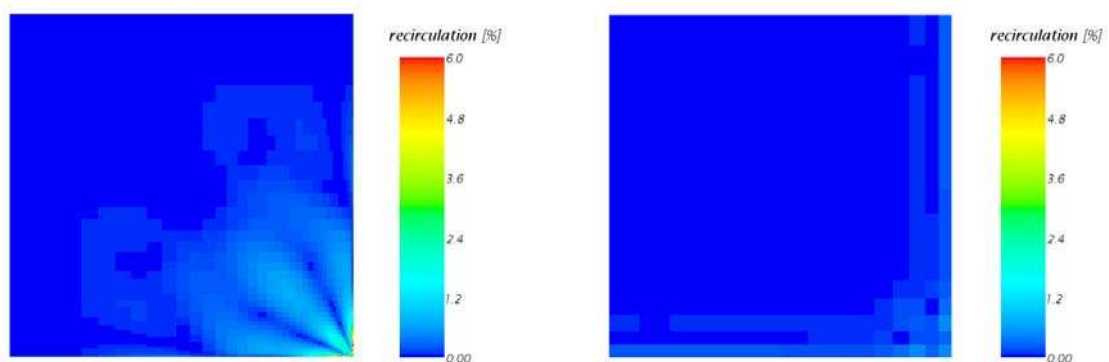


Figure 9. Secondary flow in the square duct cross-section calculated using the EB-RSM and the high Reynolds number RSM (left to right).

### 4.3. Rod bundles

With respect to the previous cases considered, rod bundles involve a much more complicated flow pattern that includes mixing and recirculation between the channels. Therefore, testing of CFD models against data on rod bundles is interesting and challenging, and of particular relevance when addressing nuclear reactor thermal-hydraulics flows. Profiles of water and gas mean velocities, void fraction and the r.m.s of velocity fluctuations are presented in Figure 10 for the experiment of Hosokawa et al. (2014), where  $x$  represents the distance from the wall of the channel box on a line perpendicular to the wall and  $L$  is the side half-length of the box. Cross-sectional distributions of the void fraction are shown in Figure 11.

None of the models successfully predicts the void fraction distribution. In Figure 11, the RSM and  $k-\varepsilon$  model predictions shows peaks in the void fraction distribution in the gaps between two neighbouring rods. In contrast, experimental measurements show a minimum in the void fraction distribution in the same regions (Hosokawa et al., 2014). The void fraction distribution in the sub-channels is well-predicted, as confirmed by the profiles in Figure 10. These profiles correspond to a vertical line between the rods in Figure 11. In Figure 11, where the experiments show a minimum, the RSM and  $k-\varepsilon$  model predictions show maximum values of the void fraction. Similarly, from Hosokawa et al. (2014), the corner region in Figure 11 is a low void fraction region, whereas these models predict the maximum value of the void fraction to be located in the corner. Therefore, although the coefficients appearing in the lift and wall force models have been tested and validated over a wide range of flow conditions in pipes and in a square channel, the same coefficients are not entirely applicable when much more complex geometries such as a rod bundle are considered. On the other hand, the minimum void regions are well-reproduced by the EB-RSM, although the void fraction distribution in the sub-channels is not predicted with any degree of accuracy, this probably being due to it not accounting for any other interfacial force other than the turbulent dispersion. It must also be remembered that, although bubbles are not rigid spheres and can deform, the minimum void fraction regions were attributed by Hosokawa et al. (2014) to geometrical constraints rather than flow conditions. By including confinement effects in the closure models, the authors were indeed able to improve the accuracy of their model. Therefore, further validation against experiments using smaller bubbles, whose preferential distribution is not affected by any geometrical constraints, is desirable.

Velocity profiles are in reasonable agreement with experiment for all the three models, although the EB-RSM provides a more accurate estimation of the liquid velocity in the gaps between neighbouring rods. Consequently, the bubble velocity is over predicted in the same regions. However, this might not have a significant effect on the flow since practically no bubbles are found in these regions. Similarly to the square duct case, the EB-RSM predicts higher turbulence levels which are more in agreement with experimental data. In the wall region, however, the EB-RSM may be over predicting the turbulence peak, even if detailed measurements are not available in this region.

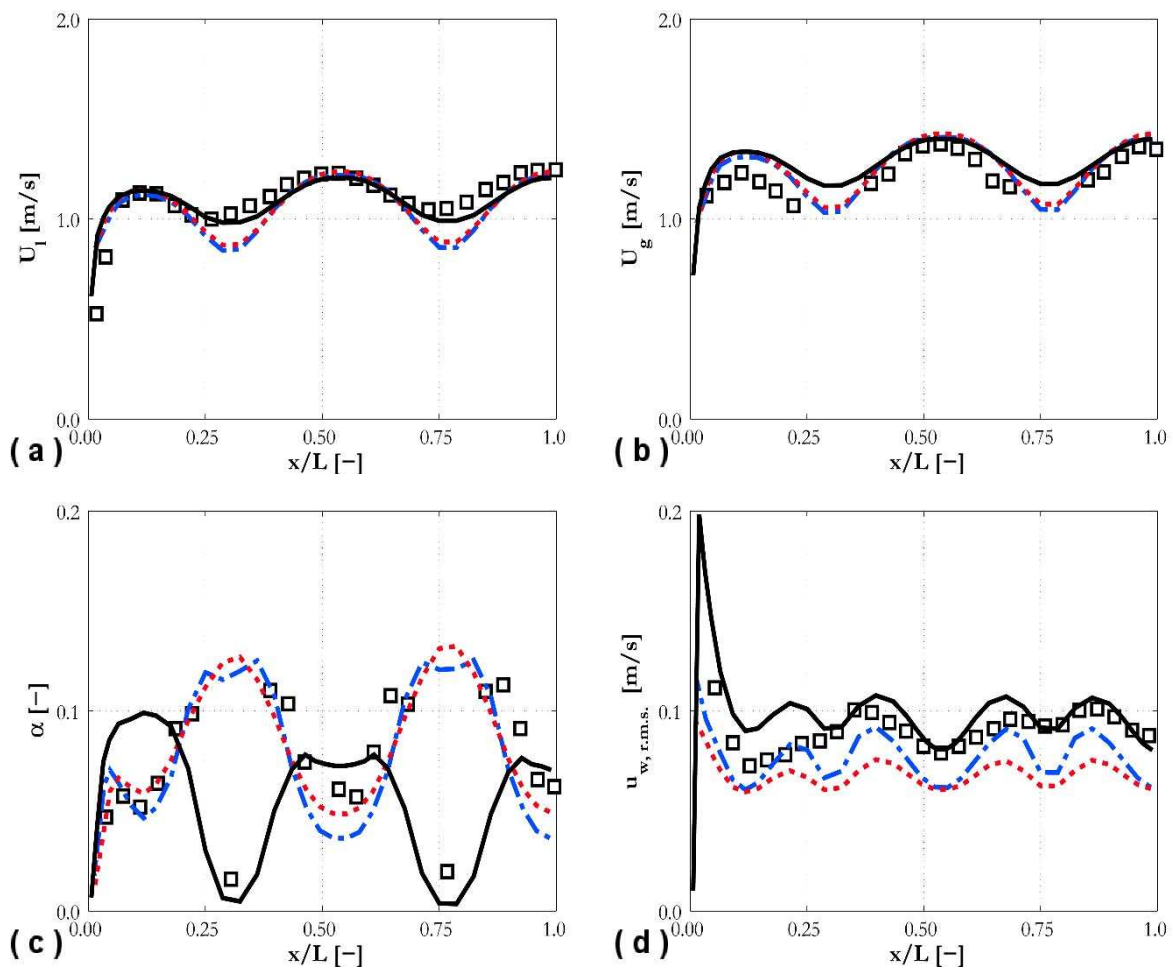


Figure 10. Predictions of (a) water mean velocity, (b) bubble mean velocity, (c) void fraction and (d) r.m.s. of streamwise water velocity fluctuations compared against the Hosokawa et al. (2014) experiment in a  $4 \times 4$  rod bundle ( $\square$  data; — EB-RSM; - - - RSM; ---  $k-\epsilon$ ). In the plots,  $x$  is the distance from the wall of the channel box along a line perpendicular to the wall and  $L$  is the side half-length of the box.

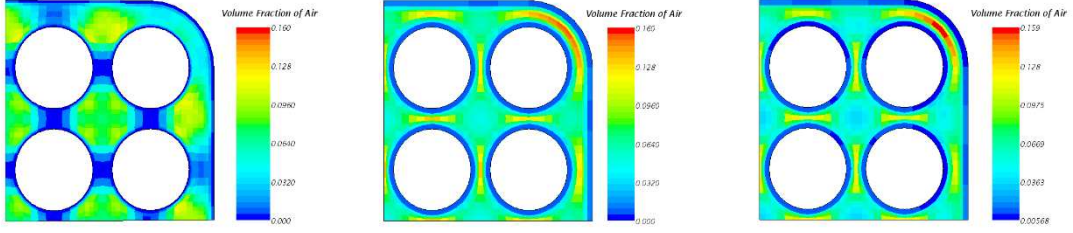


Figure 11. Void fraction distribution in the rod bundle cross-section calculated with the EB-RSM, RSM and  $k-\epsilon$  models, respectively (left to right).

## 5. Lift force modelling with the EB-RSM

In the previous section, the accuracy achieved by the EB-RSM was obtained in the absence of any lift and wall lubrication contribution. Although the robustness, if not the physical basis, of available wall lubrication models is questionable (Lubchenko et al., 2018), the lift force is still expected to decisively impact the void fraction distribution. Therefore, any bubbly flow model that aims at being accurate as well as comprehensive has to account for the action of the lift force. In view of this, the results of the previous section set the stage for the development of a more advance CFD model based on the EB-RSM for the modelling of turbulence. In this section, the lift force is added to the EB-RSM in a preliminary investigation. Fine resolution of the near-wall region prevents available lift models being directly applicable. Very high lift values are predicted in the small numerical cells adjacent to wall at a distance from the wall much smaller than the bubble diameter. Clearly, a model of this kind is not entirely physically consistent. In the absence of a physically based approach, the correlation introduced by Shaver and Podowski (2015) is adopted. The lift force is damped near the wall and approaches zero as soon as the distance from the wall becomes smaller than the bubble radius:

$$C_L = \begin{cases} 0 & y_w/d_B < 0.5 \\ C_{L0} \left[ 3 \left( 2 \frac{y_w}{d_B} - 1 \right)^2 - 2 \left( 2 \frac{y_w}{d_B} - 1 \right)^3 \right] & 0.5 \leq y_w/d_B \leq 1 \\ C_{L0} & y_w/d_B > 1 \end{cases} \quad (29)$$

The value of the lift coefficient  $C_{L0}$  has been kept equal to 0.1, consistently with the lift coefficient used for the high-Reynolds turbulence models. Comparisons for the EB-RSM with and without the lift contribution are shown in Figure 12 for the pipe flows of Hosokawa and Tomiyama (2009), Figure 12a, and Liu and Bankoff (1993a), Figure 12b. The accuracy of the model is remarkable and the impact of lift significant. The wall-peak is well predicted and the addition of lift removes the wavy behaviour in the void fraction in the centre of the pipe. It is worth mentioning that the model in Eq. (29) was also adopted in the recent work of Lubchenko



et al. (2018). However, the latter authors introduced a modification in the turbulent dispersion force to reproduce the void peak in the absence of any wall lubrication contribution. Otherwise, the void profile remained flat after the peak and towards the wall. In contrast, the resolution of the near-wall region by the EB-RSM allows reproduction of the wall peak without any additional modification.

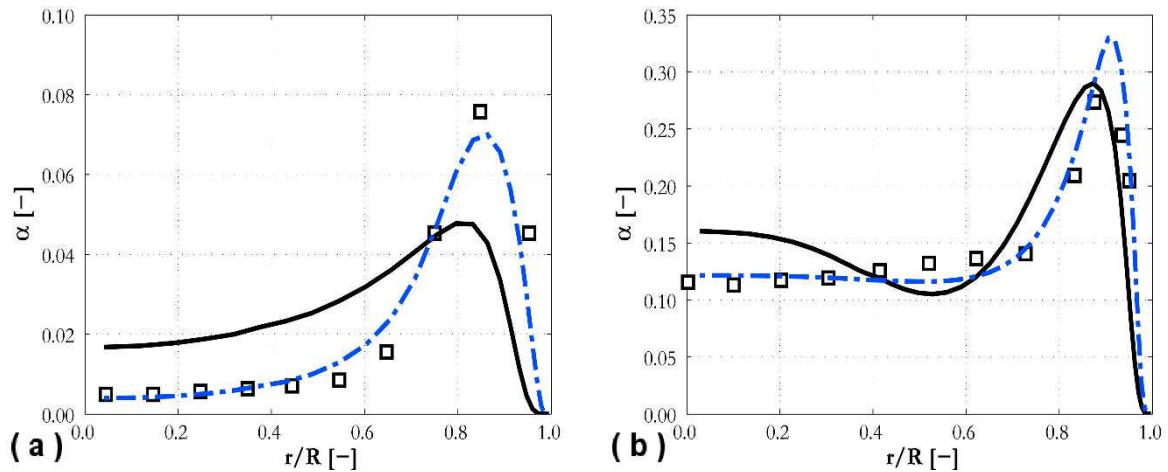


Figure 12. Void fraction profiles for (a) Hosokawa and Tomiyama (2009) and (b) Liu and Bankoff (1993a) experiments ( $\square$  data; — EB-RSM; - - - EB-RSM with lift).

Void fraction and velocity profiles for the square duct on the diagonal and parallel to the duct wall are presented in Figure 13. The accuracy of the void fraction distribution is improved and the wavy behaviour in the void fraction and velocity in the centre of the duct, which is a major drawback when lift is not accounted for, is no longer apparent when lift is included. With the addition of the lift force, flat velocity profiles similar to those predicted with the high-Re models in Figure 8 are obtained, although the velocity peak in the corner of the duct is under predicted to some extent. In the experiments, larger bubbles were found in the corner region. Therefore, improvements can be expected with the addition of a population balance model able to correctly predict the distribution of the bubble diameter in the duct cross-section.

Finally, the void fraction distribution in the rod bundle is shown in Figure 14 for the EB-RSM model with and without lift. In this case, quantitative improvement is not obtained, except for a small portion of the profile at  $x/L$  around 0.5. However, the accurate prediction of negligible void fraction in the spaces between the rods is maintained.



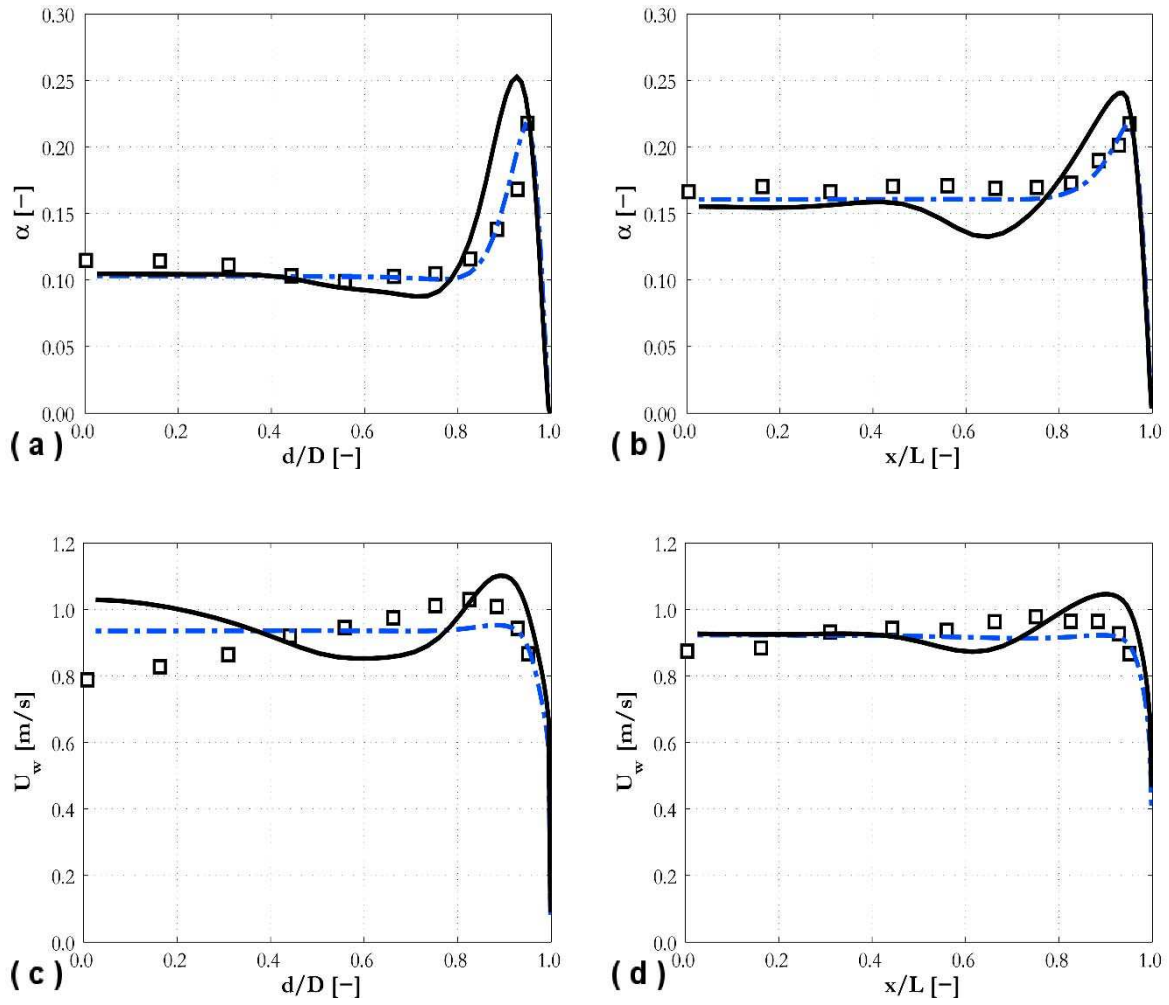


Figure 13. Predictions of (a, b) void fraction and (c, d) water mean velocity compared against the Sun et al. (2014) experiment. Profiles are shown on the diagonal (a, c) and on a line parallel to the wall (b, d) ( $\square$  data; — EB-RSM; - - - EB-RSM with lift).

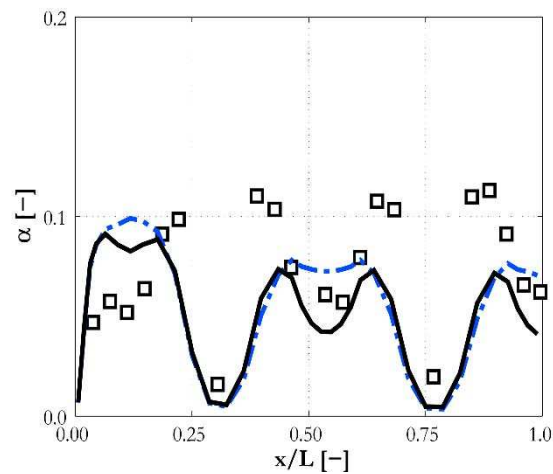


Figure 14. Predictions of void fraction compared against the Hosokawa et al. (2014) experiment in a  $4 \times 4$  rod bundle ( $\square$  data; — EB-RSM; - - - EB-RSM with lift).

## 6. Conclusions

Bubbly flows have been predicted with an Eulerian-Eulerian CFD two-fluid model closed using three turbulence models. High Reynolds number  $k-\varepsilon$  and RSM approaches, which represent current best-practice in industry and often research, using RANS approaches at least, are compared with an EB-RSM that resolves the near-wall region. The high Reynolds number models employed a common set of closures for momentum transfer, with mainly lift and wall lubrication forces determining the lateral void fraction distribution. However, lift and wall lubrication forces are neglected within the EB-RSM, with only drag and turbulent dispersion considered. The EB-RSM turbulence model has also been improved with the addition of a bubble-induced turbulence contribution to successfully predict the continuous phase turbulence field in bubbly flows. Other than for the normal pipe geometry, the accuracy of the models was additionally tested in square duct and rod bundle flows.

The main features of the flows and the void fraction distribution are well-reproduced by all three models, and even by the EB-RSM that does not account for lift and wall lubrication forces. Overall, good agreement against data is obtained, except for the rod bundle experiment. Therefore, the lift and wall force models, although having been extensively validated in pipe flows, and showing good accuracy in the square duct, are not easily extendable to a more complex geometry such as a rod bundle. Additionally, even if the accuracy of model predictions is unsatisfactory in this case, the EB-RSM predicts features of the flow which are not reproduced by the other two models.

As demonstrated by the EB-RSM predictions, the turbulence structure in the continuous phase and the induced lateral pressure distribution have a strong effect on the lateral void fraction distribution. The lift force still has a significant impact, and substantial improvements are obtained when it is added to the EB-RSM based predictions. In contrast, the wall lubrication model is unnecessary when the near-wall region is properly resolved. Overall, the present results suggest the action of turbulence has to be accurately taken into account and the near-wall region properly modelled to improve the accuracy and reliability of two-fluid models. Second-moment closures are to be preferred to two-equation, eddy viscosity-based approaches and, specifically, major improvements can be expected from the development of near-wall treatments specifically designed for two-phase flows. The present model can be used as the basis for further improving the accuracy and general applicability of CFD two-fluid models.

Inaccuracies in the prediction of the rod bundle flow suggest further improvement of the lift model that is used with the EB-RSM is necessary. Extension of the lift model to cap-bubbles, and the addition of a population balance model, will be the subject of further work to extend the model to poly-dispersed bubbly flows.

## Acknowledgements

The authors gratefully acknowledge the financial support of the EPSRC under grant EP/M018733/1, Grace Time, part of the UK-India Civil Nuclear Collaboration.

## Nomenclature

$a$	anisotropy tensor [-]
$C_D$	drag coefficient [-]
$C_L$	lift coefficient [-]
$D$	diagonal [m]
$D_h$	hydraulic diameter [m]
$D_R$	Reynolds stress diffusion flux [ $\text{J m}^{-2} \text{s}^{-1}$ ]
$d$	distance from the duct corner
$d_B$	bubble diameter [m]
$E$	bubble aspect-ratio [-]
$Eo$	Eötvös number ( $\Delta\rho g d_B / \sigma$ ) [-]
$F_d$	drag force [N]
$F_{td}$	turbulent dispersion force
$F_w$	wall force
$g$	gravitational acceleration [ $\text{m s}^{-2}$ ]
$k$	turbulence kinetic energy [ $\text{m}^2 \text{s}^{-2}$ ]
$j$	superficial velocity [ $\text{m s}^{-1}$ ]
$L$	length [m]
$L_t$	turbulent length scale [m]
$M$	interfacial momentum transfer source [ $\text{N m}^{-3}$ ]
$Mo$	Morton number ( $g\mu c 4\Delta\rho / \rho c^2 \sigma^3$ ) [-]
$P, P_k$	production of shear-induced turbulence kinetic energy [ $\text{J m}^{-3} \text{s}^{-1}$ ]
$p$	pressure [Pa]
$r$	radial coordinate [m]
$R$	radius [m]
$R_{ij}$	turbulent stress [ $\text{m}^2 \text{s}^{-2}$ ]
$Re_B$	bubble Reynolds number ( $\rho_c U_r d_B / \mu_c$ ) [-]
$r$	radial coordinate [m]
$S$	strain rate [ $\text{s}^{-1}$ ]
$S^{BI}$	bubble-induced turbulence source term [ $\text{J m}^{-3} \text{s}^{-1}$ ]
$t$	time [s]
$U$	velocity [ $\text{m s}^{-1}$ ]
$U_r$	relative velocity [ $\text{m s}^{-1}$ ]
$u$	instantaneous turbulence velocity fluctuation [ $\text{m s}^{-1}$ ]
$x$	spatial coordinate [m]
$y_w$	wall distance [m]
$W$	rotation rate tensor [ $\text{s}^{-1}$ ]

## Greek symbols

$\alpha$	volume fraction [-]
$\alpha_{EB}$	elliptic-blending function [-]
$\varepsilon$	turbulence dissipation rate [ $\text{m}^2\text{s}^{-3}$ ]
$\mu$	molecular dynamic viscosity [ $\text{Pa}\cdot\text{s}$ ]
$\mu_t$	turbulent dynamic viscosity [ $\text{Pa}\cdot\text{s}$ ]
$\nu_t$	turbulent kinematic viscosity [ $\text{m}^2\text{s}$ ]
$\rho$	density [ $\text{kg m}^{-3}$ ]
$\sigma$	surface tension [ $\text{N m}^{-1}$ ]
$\sigma_\alpha, \sigma_k, \sigma_\varepsilon$	turbulent Prandtl number for the void fraction, turbulence kinetic energy and turbulence dissipation rate [-]
$\tau$	laminar stress tensor [ $\text{Pa}$ ]
$\tau^{Re}$	turbulent stress tensor [ $\text{Pa}$ ]
$\tau_{BI}$	bubble-induced turbulence timescale [s]
$\Phi$	pressure-strain correlation [ $\text{m}^2\text{s}^{-3}$ ]

## Subscripts

$a$	air
$c$	continuous phase
$d$	dispersed phase
$g$	gas
$k$	phase k
$l$	liquid
$r$	radial direction
$w$	water
$\theta$	angular direction

## Superscripts

$g$	gas
$h$	standard away from the wall model
$l$	liquid
$w$	wall model

## Declaration of interests

None

## References

Antal, S.P., Lahey, R.T., Flaherty, J.E., 1991. Analysis of phase distribution in fully developed laminar bubbly two-phase flow. *International Journal of Multiphase Flow* 17, 635-652.

Behzadi, A., Issa, R.I., Rusche, H., 2004. Modelling of dispersed bubble and droplet flow at high phase fractions. *Chemical Engineering Science* 59, 759-770.

Besagni, G., Guedon, G.R., Inzoli, F., 2018. Computational fluid-dynamic modeling of the mono-dispersed homogeneous flow regime in bubble columns. *Nuclear Engineering and Design* 331, 222-237.

Brundrett, E., 1964. The production and diffusion of vorticity in duct flow. *Journal of Fluid Mechanics* 19, 375-394.

Burns, A.D., Frank, T., Hamill, I., Shi, J.M., 2004. The Favre averaged drag model for turbulent dispersion in Eulerian multi-phase flows, Fifth International Conference on Multiphase Flows, Yokohama, Japan, May 30 - June 4.

CD-adapco, 2016. STAR-CCM+® Version 10.04 User Guide.

Clift, R., Grace, J.R., Weber, M.E., 1978. Bubbles, drops and particles. Academic Press, New York.

Coddington, P., Macian, R., 2002. A study of the performance of void fraction correlations used in the context of drift-flux two-phase flow models. *Nuclear Engineering and Design* 215, 199-216.

Colombo, M., Fairweather, M., 2015. Multiphase turbulence in bubbly flows: RANS simulations. *International Journal of Multiphase Flow* 77, 222-243.

Colombo, M., Fairweather, M., 2016. RANS simulation of bubble coalescence and break-up in bubbly two-phase flows. *Chemical Engineering Science* 146, 207-225.

Dabiri, S., Tryggvason, G., 2015. Heat transfer in turbulent bubbly flow in vertical channel. *Chemical Engineering Science* 122, 106-113.

Daly, B.J., Harlow, F.H., 1970. Transport equations of turbulence. *Physics of Fluids* 13, 2634-2649.

Drew, D.A., Lahey Jr., R.T., 1982. Phase-distribution mechanisms in turbulent low-quality two-phase flow in a circular pipe. *Journal of Fluid Mechanics* 117, 91-106.

Ervin, E.A., Tryggvason, G., 1997. The rise of bubbles in a vertical shear flow. *Journal of Fluids Engineering* 119, 443-449.

Feng, J., Bolotnov, I.A., 2017. Evaluation of bubble-induced turbulence using direct numerical simulation. *International Journal of Multiphase Flow* 93, 92-107.

Gosman, A.D., Lekakou, C., Politis, S., Issa, R.I., Looney, M.K., 1992. Multidimensional modeling of turbulent two-phase flows in stirred vessels. *AIChE Journal* 38, 1946-1956.

Hassan, Y.A., 2014. Full-field measurements of turbulent bubbly flow using innovative experimental techniques. CASL Technical Report, CASL-U-2014-0209-000.

Hibiki, T., Ishii, M., 2007. Lift force in bubbly flow systems. *Chemical Engineering Science* 62, 6457-6474.

Hosokawa, S., Hayashi, K., Tomiyama, A., 2014. Void distribution and bubble motion in bubbly flows in a  $4 \times 4$  rod bundle. Part I: Experiments. *Journal of Nuclear Science and Technology* 51, 220-230.

Hosokawa, S., Tomiyama, A., 2003. Lateral force acting on a deformed single bubble due to the presence of a wall. *Transactions of the JSME* 69, 2214-2220.

Hosokawa, S., Tomiyama, A., 2009. Multi-fluid simulation of turbulent bubbly pipe flow. *Chemical Engineering Science* 64, 5308-5318.

Jones, W.P., Launder, B.E., 1972. The prediction of laminarization with a two-equation model of turbulence. *International Journal of Heat and Mass Transfer* 15, 301-314.

Kataoka, I., Serizawa, A., 1989. Basic equations of turbulence in gas-liquid two-phase flow. *International Journal of Multiphase Flow* 15, 843-855.

Kim, M., Lee, J.H., Park, H., 2016. Study of bubble-induced turbulence in upward laminar bubbly pipe flows measured with a two-phase particle image velocimetry. *Experiments in Fluids* 57, 55.

Lahey, R.T., Drew, D.A., 2001. The analysis of two-phase flow and heat transfer using a multidimensional, four field, two-fluid model. *Nuclear Engineering and Design* 204, 29-44.

Lahey, R.T., Lopez de Bertodano, M., Jones Jr, O.C., 1993. Phase distribution in complex geometry conduits. *Nuclear Engineering and Design* 141, 177-201.

Liao, Y., Lucas, D., 2010. A literature review on mechanisms and models for the coalescence process of fluid particles. *Chemical Engineering Science* 65, 2851-2864.

Liao, Y., Rzehak, R., Lucas, D., Krepper, E., 2015. Baseline closure model for dispersed bubbly flow: Bubble coalescence and breakup. *Chemical Engineering Science* 122, 336-349.

Liu, T.J., Bankoff, S.G., 1993a. Structure of air-water bubbly flow in a vertical pipe - I. Liquid mean velocity and turbulence measurements. *International Journal of Heat and Mass Transfer* 36, 1049-1060.

Liu, T.J., Bankoff, S.G., 1993b. Structure of air-water bubbly flow in a vertical pipe - II. Void fraction, bubble velocity and bubble size distribution. *International Journal of Heat and Mass Transfer* 36, 1061-1072.

Lopez de Bertodano, M., Lahey, R.T., Jones, O.C., 1994. Phase distribution in bubbly two-phase flow in vertical ducts. *International Journal of Multiphase Flow* 20, 805-818.

Lopez de Bertodano, M., Lee, S.J., Lahey Jr., R.T., Drew, D.A., 1990. The prediction of two-phase turbulence and phase distribution phenomena using a Reynolds stress model. *Journal of Fluids Engineering* 112, 107-113.

Lu, J., Tryggvason, G., 2013. Dynamics of nearly spherical bubbles in a turbulent channel upflow. *Journal of Fluid Mechanics* 732, 166-189.

- Lubchenko, N., Magolan, B., Sugrue, R., Baglietto, E., 2018. A more fundamental wall lubrication force from turbulent dispersion regularization for multiphase CFD applications. *International Journal of Multiphase Flow* 98, 36-44.
- Lucas, D., Beyer, M., Szalinski, L., Schutz, P., 2010. A new database on the evolution of air-water flows along a large vertical pipe. *International Journal of Thermal Sciences* 49, 664-674.
- Manceau, R., 2015. Recent progress in the development of the elliptic blending Reynolds-stress model. *International Journal of Heat and Fluid Flow* 51, 195-220.
- Manceau, R., Hanjalic, K., 2002. Elliptic blending model: A new near-wall Reynolds-stress turbulence closure. *Physics of Fluids* 14, 744-754.
- Mimouni, S., Archambeau, F., Boucker, M., Lavieville, J., Morel, C., 2010. A second order turbulence model based on a Reynolds stress approach for two-phase boiling flows. Part 1: Application to the ASU-annular channel case. *Nuclear Engineering and Design* 240, 2233-2243.
- Mimouni, S., Lavieville, J., Seiler, N., Ruyer, P., 2011. Combined evaluation of second order turbulence model and polydispersion model for two-phase boiling flow and application to fuel assembly analysis. *Nuclear Engineering and Design* 241, 4523-4536.
- Nguyen, V.T., Song, C.H., Bae, B.U., Euh, D.J., 2013. Modeling of bubble coalescence and break-up considering turbulent suppression phenomena in bubbly two-phase flow. *International Journal of Multiphase Flow* 54, 31-42.
- Ohkawa, K., Lahey Jr., R.T., 1980. The analysis of CCFL using drift-flux models. *Nuclear Engineering and Design* 61, 245-255.
- Prince, M.J., Blanch, H.W., 1990. Bubble coalescence and break-up in air-sparged bubble columns. *AIChE Journal* 36, 1485-1499.
- Rzehak, R., Krepper, E., 2013. CFD modeling of bubble-induced turbulence. *International Journal of Multiphase Flow* 55, 138-155.
- Santarelli, C., Frohlich, J., 2015. Direct numerical simulations of spherical bubbles in vertical turbulent channel flow. *International Journal of Multiphase Flow* 75, 174-193.
- Santarelli, C., Frohlich, J., 2016. Direct numerical simulations of spherical bubbles in vertical turbulent channel flow. Influence of bubble size and bidispersity. *International Journal of Multiphase Flow* 81, 27-45.
- Serizawa, A., Kataoka, I., Michiyoshi, I., 1975. Turbulence structure of air-water flow bubbly flow-I. Measuring techniques. *International Journal of Multiphase Flow* 2, 221-233.
- Speziale, C.G., Sarkar, S., Gatski, T.B., 1991. Modelling the pressure-strain correlation of turbulence: An invariant dynamical system approach. *Journal of Fluid Mechanics* 227, 245-272.

Sugrue, R., Magolan, B., Lubchenko, N., Baglietto, E., 2017. Assessment of a simplified set of momentum closure relations for low volume fraction regimes in STAR-CCM+ and OpenFOAM. *Annals of Nuclear Energy* 110, 79-87.

Sun, H., Kunugi, T., Shen, X., Wu, D., Nakamura, H., 2014. Upward air-water bubbly flow characteristics in a vertical square duct. *Journal of Nuclear Science and Technology* 51, 267-281.

Talley, J.D., Worosz, T., Kim, S., 2015. Characterization of horizontal air-water two-phase flow in a round pipe. Part II: Measurement of local two-phase parameters in bubbly flow. *International Journal of Multiphase Flow* 76, 223-236.

Tomiyaama, A., Celata, G.P., Hosokawa, S., Yoshida, S., 2002a. Terminal velocity of single bubbles in surface tension dominant regime. *International Journal of Multiphase Flow* 28, 1497-1519.

Tomiyaama, A., Kataoka, I., Zun, I., Sakaguchi, T., 1998. Drag coefficients of single bubbles under normal and micro gravity conditions. *JSME International Journal Series B Fluids and Thermal Engineering* 41, 472-479.

Tomiyaama, A., Tamai, H., Zun, I., Hosokawa, S., 2002b. Transverse migration of single bubbles in simple shear flows. *Chemical Engineering Science* 57, 1849-1858.

Troshko, A.A., Hassan, Y.A., 2001. A two-equation turbulence model of turbulent bubbly flows. *International Journal of Multiphase Flow* 27, 1965-2000.

Ullrich, M., Maduta, R., Jakirlic, S., 2014. Turbulent bubbly flow in a vertical pipe computed by an eddy-resolving Reynolds stress model, 10<sup>th</sup> International ERCOFTAC Symposium on Engineering Turbulence Modelling and Measurements (ETMM 10), Marbella, Spain, September 17-19.

Vasavada, S., Sun, X., Ishii, M., Duval, W., 2009. Benchmarking of the one-dimensional one-group interfacial area transport equation for reduced-gravity bubbly flows. *International Journal of Multiphase Flow* 35, 323-334.

Wang, S.K., Lee, S.J., Jones, O.C., Lahey, R.T., 1987. 3-D turbulence structure and phase distribution measurements in bubbly two-phase flows. *International Journal of Multiphase Flow* 13, 327-343.

Welleck, R.M., Agrawal, A.K., Skelland, A.H.P., 1966. Shape of liquid drops moving in liquid media. *AIChE Journal* 12, 854-862.

Woldesemayat, M.A., Ghajar, A.J., 2007. Comparison of void fraction correlations for different flow patterns in horizontal and upward inclined pipes. *International Journal of Multiphase Flow* 33, 347-370.

Yao, W., Morel, C., 2004. Volumetric interfacial area prediction in upward bubbly two-phase flow. *International Journal of Heat and Mass Transfer* 47, 307-328.



Yeoh, G.H., Tu, J.Y., 2006. Two-fluid and population balance models for subcooled boiling flow. *Applied Mathematical Modelling* 30, 1370-1391.